TECHNISCHE UNIVERSITÄT MÜNCHEN
Aus dem Fachgebiet Neuropathologie
(Leitung: Univ.-Prof. Dr. J. Schlegel)
des Instituts für Allgemeine Pathologie und Pathologische Anatomie
(Direktor: Univ.-Prof. Dr. H. K. Höfler)

Label-free microscopic bioimaging by means of confocal Raman spectroscopy on living glioblastoma cells

Katharina Christiane Klein

Vollständiger Abdruck der von der Fakultät für Medizin der Technischen Universität München zur Erlangung des akademischen Grades eines Doktors der Medizin genehmigten Dissertation.

Vorsitzender:
Univ.-Prof. Dr. E. J. Rummeny

Prüfer der Dissertation:
1. Univ.-Prof. Dr. J. Schlegel
2. Univ.-Prof. Ph.D. V. Ntziachristos
3. Univ.-Prof. Dr. B. Hemmer

Die Dissertation wurde am 08.12.2011 bei der Technischen Universität München eingereicht und durch die Fakultät für Medizin am 30.01.2013 angenommen.

Table of contents

List of figures

List of abbreviations

Ab	antibody
Ad	adenine
aIF	artificial immunofluorescence (image)
CARS	coherent anti-Stokes Raman scattering
CCD	charge-coupled device
COX	Cytochrome-C-oxidase
Cy	cytosine
Cys	cysteine
DAPI	4',6-Diamidin-2-phenylindol
DMEM	Dulbeccos modified eagle's medium
DNA	desoxyribonucleic acid
ER	endoplasmic reticulum
rER	rough endoplasmic reticulum
sER	smooth endoplasmic reticulum
FITC	Fluorescein isothiocyanate
FT	Fourier-transformed
GFP	green fluorescent protein
Gu	guanine
IF	immunofluorescence
IR	infrared
kD	kilo Dalton
LN	Lausanne
NA	numerical aperture
Nd:YAG	neodymium-doped yttrium aluminium garnet
NIR	near infrared
PBS	phosphate-buffered saline
PCA	principal component analysis
Phe	phenylalanine
RGB	red-green-blue
ρ	correlation coefficient *rho*

$\bar{\rho}$	mean correlation coefficient
RNA	ribonucleic acid
rRNA	ribosomal ribonucleic acid
SERS	surface-enhanced Raman scattering
SHG	second harmonic generation
SNARE	soluble N-ethylmaleimide-sensitive-factor attachment receptor
Th	thymine
Trp	tryptophane
Tyr	tyrosine
Ur	uracil
UV	ultraviolet
WHO	world health organisation

1 Introduction

For histological examinations on tissues, different methods have been established. Besides routine staining methods, immunohistochemistry, immunofluorescence, or destructive biochemical methods, such as electrophoresis or blotting, are commonly used. Most of these methods require the use of dyes for direct imaging, or specific markers for immunohistochemical or immunofluorescent labelling. Due to their destructiveness or the usage of stains, they impede further usage of the specimen.

In cell culture as well, most established methods for imaging of subcellular structures are invasive due to the necessity of fixation or freezing, or the use of dyes or marker particles, e.g. electron microscopy, cryoelectron microscopy, or fluorescent staining. Other methods require lysis or extraction of intracellular material. Due to the destructiveness of these methods, similar problems concerning further usage of the cells or monitoring over a certain period of time, arise [71, 94].

In (bio)physics, materials sciences, and engineering, a set of noninvasive imaging techniques has been developed. Besides Fourier-transformed infrared (FT-IR) spectroscopy, multiphoton microscopy, or atomic force microscopy, methods such as Raman spectroscopy have become more and more commonly used analytical techniques [87]. Complementary with the absorption based IR spectroscopy, Raman spectroscopy is a spectroscopic technique that analyses the inelastically scattered, spectrally shifted light from a monochromatic light source. The measurement of the photon's energy loss (or gain, depending on the method) gives specific information on local vibrational states of the sample material. With technical improvements, such as a confocal setup, the volume from which scattered light is detected can be controlled. Thus, a resolution on a sub-micrometer scale can be achieved. The information extracted of such small volumes make the method very sensitive for material discrimination and useful for different evaluations in materials sciences [35].

Over the past decades, a number of such techniques have been refined to fulfill the requirements of biochemical, biotechnical [14, 51], and medical investigations [18, 36]. At first, the two complementary vibrational spectroscopic techniques, IR spectroscopy and

Raman spectroscopy, seemed most promising, with different advantages and disadvantages [25, 60]. When imagining experiments under cell culture conditions, such as on single living cells, Raman microspectroscopy offers a major benefit, which is its applicability in aqueous media such as PBS [73, 94, 95], thereby leaving the environment of the cells as close to cell culture as possible. In addition, higher spatial resolutions can be achieved when using lasers in the visible range [62].

For a long time, the experts' opinion on laser wavelengths applicable for biological material was determined, especially regarding living objects (mainly protozoa and cultured cells). Monochromatic lasers emitting light of the near-infrared spectrum (NIR) were used, mainly in wavelengths of between 650 nm and 785 nm and laser powers of 70 – 250 mW [51, 65, 73, 81, 94, 98–100]. The decisive factor for this was a finding of the group around G. J. Puppels which showed that living cells are damaged when investigated with Raman systems using lasers in the range of visible light, but not when using lasers of the near-infrared spectrum [80]. Recently, the validity of this statement has been challenged. C. Matthäus et al. applied Raman spectroscopy on single cells at an improved spatial resolution, using a green laser of a wavelength of 488 nm at a laser power of 30 mW [63]. This was confirmed by futher research [38]. Raman systems coupled to lasers of shorter wavelength offer a number of advantages such as shorter integration times per point, lower laser powers for comparable spectral quality, and a higher spatial resolution. In addition, when using low laser powers (< 30 mW), no autofluorescence or changes in the specimen are observed.
The inconsistent answers to the question about the laser wavelength suggest an individual choice according to the requirements of the problem [16]. In our case, one main issue is a good optical resolution on a subcellular level.

After certain subcellular structures could be identified in fixed cells [62, 63], a number of intracellular compartments remained to be scanned and analyzed to get a more complete picture of the spectroscopical characteristics of single cells. Besides mitochondria, which have shown to be detectable by Raman microspectroscopy [63], the following intracellular structures form substantial parts of the (tumor) cell, participate in shaping, and contribute to its replication rate: the prominent nucleus is surrounded by the membraneous compartments, i.e. the endoplasmic reticulum, which continues into the Golgi network. The filamentous system, such as microfilaments and thin filaments, provides stability in the cell's three-dimensional structure.

In this thesis, the following issues shall be examined: The theoretical background of Raman microspectrosopy and its applications will be overviewed in chapter 1.1. Immunofluorescence microscopy, the current gold standard for subcellular imaging, which we use for

direct comparison with the Raman data, will be explained in chapter 1.2. Here, also the subcellular structures under investigation and the maker particles chosen will be described. Chapter 1 ends with a short outline of the experimental concept.
Chapter 2 gives a descriptive overview of the setup and the sequence of the experiments. Exact listings and protocols are provided in the appendices B and C. The results of both imaging techniques and the mathematical approaches for data matching and extraction of important information from Raman datasets with the help of direct comparison with the results obtained with IF microscopy are explained in chapter 3. The spectroscopical features and the feasibility of a comparison between both methods, shown for each respective subcellular structure, will be discussed in chapter 4. Chapter 5 (and chapter 6 in German, respectively) gives a summary of the work.

1.1 Raman spectroscopy

Raman spectroscopy can provide detailed information about the chemical composition of a sample. It analyses Raman scattered photons, i.e. spectrally shifted, inelastically scattered light. The principle of Raman scattering was first described in 1928 by the Indian physicist Chandrasekhara Venkata Raman as "a new type of secondary radiation" [84], for which he received the Nobel Price for physics two years later [31]. At the same time, the Russian physicists Grigori S. Landsberg and Leonid I. Mandelstam reported similar observations [50]. But only with the invention of lasers as intense and monochromatic light sources, Raman spectroscopy became a widely applicable technique [40], first in materials sciences, and later on also in fields of biotechnology and bioanalysis.

1.1.1 Interactions of light and matter

When light irradiates matter, different processes might occur. Most commonly, the photons can be transmitted or reflected. Another possible interaction is the absorption of photons leading to an excited electronic state of the matter, which occurs when the photon energy matches a real state of a molecule. The excited molecule relaxes to the ground state in a certain time by a radiative process (e.g. fluorescence) or non-radiative processes (e.g. generation of heat). IR- spectroscopy probes such interaction to analyze specimen by means of absorption.

Another type of interaction is scattering, which occurs when the photon energy does not match a real state. If the photon energy is conserved during scattering, the process is called elastic. There are two main types of elastic scattering processes, Rayleigh and Mie scattering, depending on the relation between wavelength and scattering particle size. Elastic scattering can be considered as an absorption of the photon, a transfer of the molecule into a virtual intermediate state, followed by an immediate relaxation into the ground state with re-emission of the photon. When observing scattered light, the elastic scattering usually comprises a large percentage (99,99%).

1.1.2 The Raman effect

The Raman effect is a nonlinear inelastic scattering effect which involves molecular vibration (e.g., bending or rotation; in crystals the interacting vibrational modes are called phonons) [103] (chapter 1), [35]. When energy is transferred from or to the scattering

photon, this is called inelastic scattering. Functional groups are excited to a virtual intermediate state, but relax to a vibrational state above the ground state. As a result, the scattered photon has a lower energy than the incident one (red shift or Stokes shift). However, if an incident photon interacts with a molecule already excited to a vibrational state, it is also excited to a virtual intermediate state and can relaxe to its ground state. Therefore, the energy of the scattered photon is higher than the energy of the incident photon. Thus, the scattered photon has a shorter wavelength (blue shift or anti-Stokes shift) [103] (p. 1f, p, 11ff), [58] (p. 5 - 10).

Stokes and anti-Stokes shift are symmetric with respect to the wavelength of the irradiating light. Both are determined by the energetic difference between ground and vibrational state. Still, the probabilities for their occurrence are different. At ambient temperature, the anti-Stokes process occurs less often than the Stokes shift according to the Boltzmann's rule, giving the occupation of the energy levels for a certain temperature. A schematic overview on the Stokes Raman shift is given in Figure 1.1.

Energetic changes can be displayed as a spectrum of the scattered light, representing the

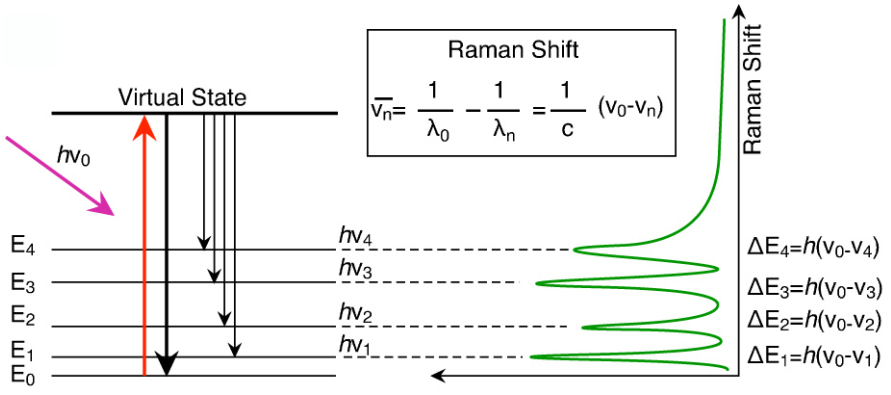

Figure 1.1: *The Raman shift.*
Electrons are transferred to a virtual molecular level by incident photons. The energy transfer causes a loss of energy in the photons. The electrons later on relax through different vibrational transitions which are specific to the material. The peaks of Raman shifted photons are measured in the Raman spectra. They show high chemical and structural sensitivity [81].
Disambiguation:
E_i: *energy levels*
ΔE_i: *energy difference between the* i^{th} *and the ground state*
h: *Planck's constant* ($h = 6,62606957 \times 10^{-34} Js$)
ν: *photon frequency*
ν_i: *photon frequency, proportional to the energy needed to reach the* i^{th} *energy state,*
λ: *wavelength*
The energy of the photon $E = h\nu$.

energy shifts in relation to the incident wavelength. This spectrum gives specific information on the material composition, since the energy shift is characteristic for the chemical groups in the material [39], [58] (p. 5 - 6).

The basic difference between IR- and Raman spectroscopy are the selection rules, that state a vibration to be Raman active or infrared active. For infrared activitity, the material has to change its permanent dipole moment during the oscillation. For Raman activity, there has to be a change in the polarizability during the oscillation. This means, that if a vibration is Raman active, this vibration will be silent in infrared and vice versa [81].

In summary, a spectrum observed from scattered monochromatic light will show three features:

1. the Rayleigh peak, at the same energy level than the incident light beam (0.01%)[1]
2. inelastically scattered photons which lose energy, thus show a longer wavelength than the incident light, the Stokes shift (10^{-6}%)
3. inelastically scattered photons which gain energy, thus show a shorter wavelength than the incident light, the anti-Stokes shift ($< 10^{-6}$%)

In our spectroscopic setup, as described in section 1.1.3, besides the residuals of the Rayleigh peak after filtering[2], the Stokes photons are measured, as it is done in most of the common Raman techniques [3].

1.1.3 Optics and resolution

The optical system to record Raman scattered light usually consists of three main parts: a single mode laser as the intense light source, a spectrometer to analyse the scattered light and a microscope for focusing and collecting the light. The laser beam is guided to the microscope with an optical fiber, where the laser is focused on the sample through an objective. In parallel, a common microscope illumination is used for an optical inspection of the sample. The scattered light, collected with the same objective as used for focusing, is led over a multimode fiber into a spectrometer, where it is splitted into its spectral components with a diffraction grating and recorded by a charge-coupled device (CCD) sensor.

[1] After application of an edge filter, 99,99% of the elastically scattered light is eliminated.

[2] Despite using an edge filter to eliminate the Rayleigh peak, a certain amount of Rayleigh signal will always remain due to its relative strength in comparison to the much weaker Raman photons.

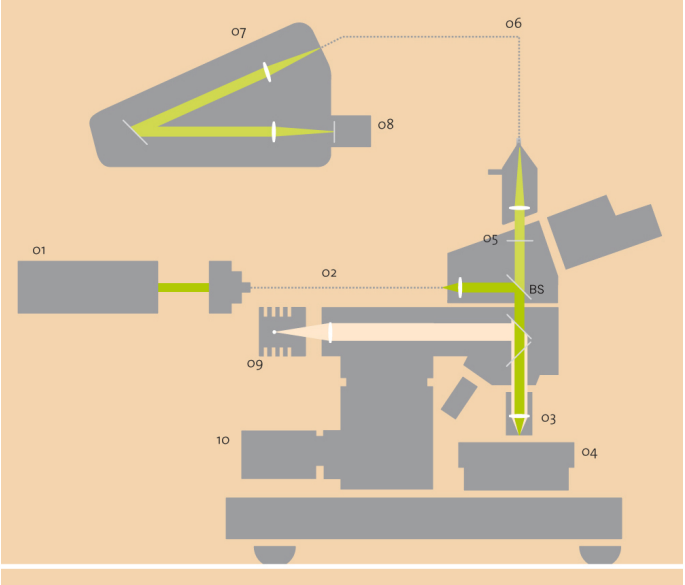

Figure 1.2: *Spectroscopical setup (courtesy of WITec, Ulm, Germany)*

The setup of the WITec Raman microscope used for this work is shown in figure 1.2. The laser beam, emitted by a frequency-doubled neodymium-doped YAG laser (01) is coupled to the microscope over a single mode fiber. Parallel to it runs the white light beam (09). Both can be focused through an objective (03) on a piezo-driven sample stage (04). With a mirror, the white light beam is then directed into the eyepiece. The scattered laser light is filtered with an edge filter (05) and focused into a multi mode fiber (06), which leads to the spectrometer. This multimode fiber with a core diameter of 50 µm acts as pinhole to achieve the confocal set for controlling the focal depth where the scattered light is recorded. In the spectrometer, the light is split into its spectral components using a dispersive grating with a 600 mm^{-1} line density (07) and recorded by a CCD system (08) [106].
By adjusting the optical components (objective and pinhole), the resolution is of the order of 1 μm^3. The vibrations give specific information of this small volume. Crystals, which consist of symmetrically repetitive chemical structures, usually show very well-defined peaks, while complex chemical constituents, as found in biological samples, will show spectra with blended lines. With a better spatial resolution, this information might become more and more precise, crossing the line between heterogeneity on the coarse scale and homogeneity on the fine scale [19].

The spatial resolution depends on the scattering volume [35]. Optically, this mainly depends on the magnification and the point spread function of the optical components and the CCD detector. The point spread function describes how different mechanisms, such as diffraction, reflection, or aberration influence the recorded shape of a point-like signal. In the confocal setup, a pinhole limits the field of collection and reduces the spatial and axial contributions from outside the focal ellipse to the background signal to a minimum. Choosing a certain pinhole diameter allows to select the axial focus (focal depth) [75] (p. 4 - 5).

The spectral resolution, on the other hand, is given by the design of the spectrometer setup and the grating used as the dispersive element splitting up the light into its spectral components.

1.1.4 Raman spectroscopy in bioanalytical fields

With the development of high-quality laser devices, Raman spectroscopical techniques were primarily used in different branches of materials sciences. Traditionally, its domains are the investigation of geomaterials (gems, rocks, ceramics and more) [87], research in catalysts [89], historical objects [30], and works of art [101]. Applications in bioanalytical fields started with purified biochemical samples, such as cytochrome C [91] or hemoglobin [92]. Afterwards, the technique has been applied to a number of extracted biochemical substrates. After experiments on viable erythrocytes have been carried out in 1988 [41], in 1990 the group of G. J. Puppels were the first to analyze single living cells and chromosomes [78]. They extended those first experiments on single granulocytes [79] and found that, with their setup, sample degradation occurred when using a laser in the range of visible light, but not with a laser of the NIR range [80]. Until recently, this remained to be the leading opinion [16, 51].

Raman spectroscopy has a number of properties which make it favorable for use in bioanalytical fields and investigations on single, even living, cells. It can be applied to materials in the most different physical states, e.g. solutions, gels, films, solids. Measuring times have become sufficiently short for life cell imaging through technical improvement of the setup [95]. The volume which is measured can be very small, and with microscopes which provide a confocal setup, the optical resolution is approaching the physical limit [18]. Raman spectroscopy is a non-destructive method. Further, it does not require any labels or dyes, and is therefore a technique of rising importance for medical research, e.g. in molecular pathology [3, 95]. Generally, investigations on biological specimen can be carried out in two different ways. One spectrum, providing a chemical ”survey“ of the material, can be recorded by integrating over a large focal field. This is of use e.g. when looking for quick discrimination between cells of different cell lines. Alternatively, many spectra with very small focal areas can be recorded, resulting in a map which provides an insight in substructures of the sample. On a piezo-driven scanning stage, a determined field of view can be raster-scanned point by point with a very small spatial distance. This results in a so-called Raman hyperspectral image [16], which means that for each scanning point one spectrum is recorded. Resolutions of these images in x,y can be as low as 325 nm, using green light for illumination.

Since the beginning of investigations on biological specimen, large databases for the assignments of chemical, biochemical and biological samples have been published [21, 22, 43, 62, 63, 71, 79, 90, 95]. Appendix A gives an overview on the most frequently observed spectral features and their assignments to biological samples and cells, as it is of relevance for this work.

In microbiology, Raman spectroscopical methods have been used for classification and identification of microorganisms [48, 60, 61], studies on yeast [59], fungal spores [23], virus capsid assemblies and whole viruses [95]. Intrinsic photo-bleachable pigments have been used for discrimation of bacterial stems [85]. In biochemistry, applications range from investigations of proteins and nucleic acids to the investigation of protein-ligand complexes, protein secondary structure, misfolding, and monitoring of enzyme systems [14].

Medical applications of Raman spectroscopy are quickly expanding. A large number of studies have been performed on tissues, often comparing healthy with cancerous specimen, such as blood cells[79], skin [15, 32], bone [46, 110], breast [37], cervical [43], and axillary lymph node tissue [42]. Broad investigations have been carried out on tissue of the brain and different types of brain cancer [2, 4, 32, 53–56]. In parallel, the diagnostical and clinical implementation of Raman spectroscopy is rising [18, 36, 73], which became possible with the development of equipment allowing in vivo Raman spectroscopy. For example, a Raman endoscopical setup has been used to diagnose benign and malign lesions of the stomach in vivo [8].

In cell biology the use of Raman microspectroscopy has been extended to various applications. Different intracellular compartments have been illustrated: first works showed the protein distribution in single cells [98] and protein and DNA distribution in apoptotic cells [97], later on the nucleus and chromatin [62], lipid bodies [52, 100] and mitochondria [63] were imaged. Recently, specific peaks occuring in mitochondria could be deciphered [77].
Spectral differences between living and dead cells have been investigated already in 2003 [72]. In the following times, different states of cellular stress [52] and cell death have been monitored [81, 102]. Recent works have been performed to evaluate the effects of fixation on cells [29, 65].
Dynamic imaging of living cells has been carried out to investigate time-dependent cellular processes, such as RNA translation [70], different states of mitosis [62] and of the cell cycle in general [93], and to monitor the molecular distribution of a number of substances (water, cytochrome c, protein beta sheeds, lipids) [34, 38, 108]. Recently, even small structures such as immunological synapses have been depicted [111].

The possibilities of dynamic imaging are as well very interesting for pharmacology and toxicology. In 2004, the group of I. Notingher showed that a continuous imaging of biochemical changes in single cells induced by pharmaceuticals is possible. Later on, different experiments have been conducted in this field [73], e.g. to trace intracellular drug carrier systems [64].

With technical improvements, which provide an easier handling and reduce investigation times as well as laser power immensely, Raman microspectroscopy became applicable for investigations on stem cells with good results [16, 112]. Another new approach is, to combine a Raman setup with optical traps for cell identification in fluids [27]. With further improvements regarding measurement times, experimental setups for Raman-driven cell sorting might become possible [74]

Besides nonresonant, spontaneous Raman spectroscopic imaging, other Raman spectroscopical methods have been applied in bioanalytical fields. These techniques range from complicated, custom-built setups [99] to established devices in material sciences, such as coherent anti-Stokes Raman scattering microscopy (CARS) [17], surface-enhanced Raman scattering (SERS) with nanoparticles [47], or stimulated Raman scattering microscopy [32]. For a review of these Raman techniques and their applications in life-sciences, see [3, 71, 94].

1.2 Fluorescence microscopy

The aim of this work is, to show that an intracellular mapping of the most prominent structures of a cultured cell by Raman microspectroscopy is feasible. To do so, a standardized method must be used to give a reliable system for comparison, which is also suited for computerized image overlay and data matching. Currently, fluorescence microscopy is a gold standard for the visualization of intracellular components. According to the experimental setup described in chapter 2, we performed immunofluorescence imaging directly after Raman data acquisition, to enable a direct comparison and give a reliable reference for the intracellular compartments we focus on. In the following, the method is sketched and the choice of markers will be explained with respect to their cell-biological properties.

1.2.1 Basic principles of fluorescence microscopy

Fluorescence is a phenomenon that only occurs in certain agents, or probes. After being irradiated with light of a certain wavelength, they emit light which shows a longer wavelength. The principle underlying this effect is similar to the one occuring in Raman scattered light: the difference in energy between the excited and the emitted light is also called Stokes shift.

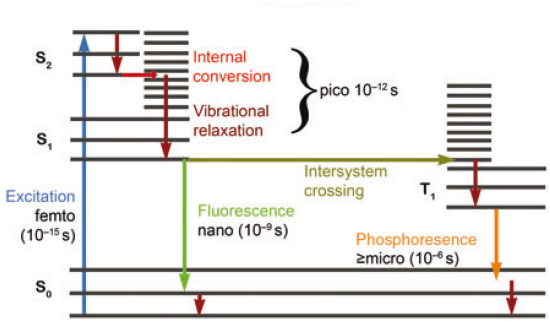

Figure 1.3: *Principles of fluorescence: the excitation light (blue arrow) lifts an electron into an excited state. It relaxes in different ways, emitting fluorecence light of lower wavelength then the incident light (green arrow). Note the timeframes.[57]*

Here, an electron of the fluorescing substance gets lifted to a higher energy level. It looses this energy mainly in two steps: First, a vibrational relaxation occurs, which brings the photon to a lower orbital state. From here, it secondly looses a specific amount of energy to the ground state, and emits the fluorescent light. Figure 1.3 illustrates the transition between energy levels in the molecule. The time scale in which these physical processes occur is very short (see figure 1.3), and the intensity of the emitted light is reduced by orders of magnitudes in comparison to the incident light.

In a setup of a reflected light microscope (epifluorescence microscope) the emitted light can be led to a spectrally sensitive detector. The beam path of this setup is shown in figure 1.4.

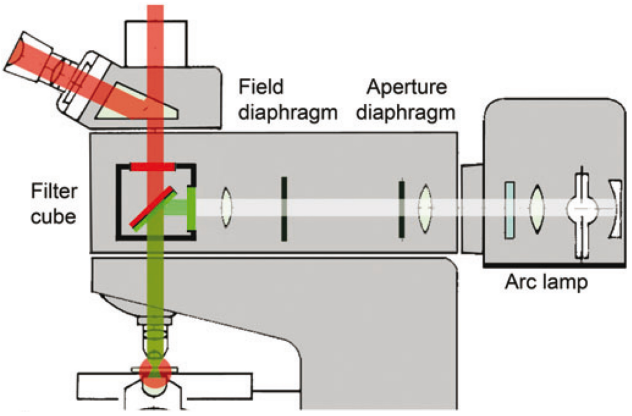

Figure 1.4: *Epi-Fluorescence microscopical setup. The incident light is directed to the focal plane through a dichroic mirror (beam splitter). Emitted light will be directed through the beam splitter to the detector, after a barrier filter blocks out the illuminating light. [57]*

An arc lamp is used as a white light source. Through a filter cube, only certain wavelengths (here shown green) will be filtered to illuminate the specimen on the microscopy table. They are directed onto the sample by a dichroic mirror and focused by a lens. Both are reflected and fluorecent light reaches the beam splitter trough the same objective. It arrives at the filter cube, which consists of two parts. Besides the dichroic mirror, there is a barrier filter which filters out the reflected excitation light beam (green) and only lets the fluorescent light pass (shown in red). By a sensitive detector, even very low amounts of fluorescence can be detected. This also means, that in this microscopy mode, the specimen itself converts the light which is later on detected [57, 88]. As a result of the complete filtering of the incident light, the background noise is reduced to a minimum, which makes the method highly specific for the fluorescent probe. Only a small range of wavelengths around the intrinsic wavelength of the fluorescing particles themselves will be recorded, the rest of the spectrum is blocked out.

There is a number of fluorescing agents, many of which occur in nature, such as the green fluorescent protein (GFP), which was first discovered in 1962 [86]. Through structural analyses of this protein, the nature of its fluorescence could be better understood. Spectral features were investigated and, subsequently, a number of fluorophores were developed, which showed similar features. Synthetic fluorophores are molecularly designed in a way, that they contain a recognition sequence, whose counterpart is expressed on an antibody which specifically targets a structure of interest [107]. Thus, synthetic fluorophores can be bound to any antibody as long as this antibody fits the analogue recognition sequence. Today, fluorophores are commercially offered for different colors, so that different parts of a specimen can be visualized simultaneously. According to the spectral range of the fluorescent protein, appropriate filters have to be chosen for the microscopical detection. Since the group of different fluorophores is large, only the ones of interest for this work

are described here.

Fluoresceinisothiocyanat (FITC) is a protein which was developed from the fluorescent dye fluorescein[3]. When excited with blue light, it emits green light. Rhodamin[4], another fluorophore used in this work, emits red light after excitation with a blue-green light source. Typically the last fluorophore imaged is 4',6-Diamidin-2-phenylindol (DAPI)[5], because it is excited by UV light, which might cause photodamage on the other fluorophores. DAPI emits light of blue color [45]. Using these three fluorophores, classical three-channel red, green, and blue (RGB) pictures can be recorded.

As mentioned above, fluorophores undergo photochemical reactions when being excited, which means that fluorecence fades with time of excitation. This effect is called photobleaching [57, 88]. To avoid excessive bleaching, the excitation light powers, as well as exposure times, have to be kept at a low level. In addition, excessive incident light power can also excite fluorophores which are actually out-of-focus, and therefore reduce the optical resolution [13].

1.2.2 Intracellular compartments and antibodies used for fluorescence imaging

Given a three-channel (RGB) imaging setup, only a limited number of compartments can be visualized at once. Therefore, the first consideration is, which subcellular structures are most important for cellular functions. This depends, besides other influences, largely on the type of cell. All experiments described in this work are performed on human glioma cells, LN-18 [26]. They are characterized by a high replication rate in cell culture and respectively, quick growth as a tumor. It has to be expected that those organelles are important structures in such cells, which contribute to biosynthesis, modifications and metabolization of cellular constituents.

According to this, the following compartments have been chosen to be imaged with IF microscopy in this work: The nucleus is the main point of orientation. It is marked in all IF images, since it is a structure which also shows clearly in Raman spectral images. The nucleus is, on the other hand, initiation site for the endoplasmic reticulum (ER), one of the main endomembranous compartments, whose function is proteinbiosynthesis and synthesis of lipids. It produces large fractions of the constituents of the intracellular organelles

[3]FITC is chemical substrate in PubChem with the CID: 18730. Here, detailed information on chemical structure, classification, use and a number of secondary literature is provided.
[4]PubChem CID: 13806
[5]PubChem CID: 2954

themselves [1] (chapter 12, p. 659ff.). The other main part of the membraneous system is the Golgi apparatus, which also governs part of the biosynthesis of proteins and lipids, and carries out most post-translational modifications [24]. In higher eukaryotic cells, the Golgi apparatus is expected in close proximity of the nucleus, similar to the ER. For a better spatial imagination, the following description might be helpful: Parts of the endoplasmic reticulum and the Golgi complex can be seen as large membraneous sheets, which are stacked into each other and communicate via their points of contact. Furthermore, the Golgi complex as well as the endoplasmic reticulum are polarized compartments, which arrange according to their function and with respect to certain microtubular structures, which play a role in cell polarity. The rough ER (rER) will more probably be located in vicinity to the nucleus, and the cis-Golgi cisternae more likely close to the rER. On the other hand, the smooth ER (sER) and the trans-face of the Golgi system are more likely to be related to the plasma membranes [12, 66, 82].
Mitochondria supply the cell with energy. They take most different shapes, from single, unattached forms up to interconnected, large tubular networks [7, 44]. Since they form a substantial part of the intracellular bodies, especially in cells with a high turnover, as are tumor cells, we decided to display them as well, although it has already been shown that they can be visualized by means of Raman microspectroscopy [63, 77].
For an exact registration of Raman and IF images, it is necessary to depict the cellular borders in the IF images. Microfilaments, built from actin polymers, are part of a dynamic network which stabilizes the cellular architecture and facilitates its motility. Leading sites of the cell, as occuring in motile cells of stellate structure as LN-18, show large bundels of actin which are anchored on certain points of adhesion [28]. Even though it is difficult to consider the filamentous skeleton of a cell as an ”organelle“ [33], the mentioned properties motivate the marking of the microfilaments in all IF images.

When dyeing the nucleus and actin filaments in all images, one color channel remains for one of the other specified organelles. In the same experimental setup, this stain (FITC) was used to mark either the endoplasmic reticulum or Golgi complex or mitochondria. To dye the nucleus and the actin filaments, commonly used stains have been chosen. DAPI, already mentioned in section 1.2.1, is a fluorophore which binds specifically to DNA. It builds complexes with nucleic acids and is a very efficient biological dye [45]. Actin filaments can be visualized by phalloidin, a member of the phallotoxin family, when coupled to a fluorophore. Phalloidin also stabilizes the actin structures towards the filamentous part [20, 104].

For the respective organelles marked in the green channel, specific antibodies have been chosen, which in the next step were coupled to FITC (see chapter 2). All antibodies des-

cribed below are commercially available.
Calnexin is a chaperone, a small (90 kD) protein positioned in the membranes of the endoplasmic reticulum. It associates with glycoproteins, which are later channeled through the endoplasmic reticulum. It plays a role in quality control and folding of these glycoproteins and is involved in stress-induced apoptosis [83, 105]. A purified anti-Calnexin antibody (Ab) has been proven suitable for immunofluorescence application [68].
The cytochrome oxidase (COX) is a large enzyme complex, building the last part of the respiratory chain on the inner mitochrondrial membrane. A deficiency in its function can lead to a number of diseases. The subunit IV of COX, an oxidoreductase, is one of the smaller subunits of the COX complex [6, 96]. For IF preparations, a monoclonal rabbit antibody that binds specifically to COX IV is most suited [69].
SNARE proteins are involved in vesicle trafficking and transport. Syntaxin 6 is a member of the Syntaxin family, a subfamily of these SNARE proteins. It is an internal membrane protein of the Golgi apparatus and is widely expressed in different tissues, including the brain [10, 11]. A monoclonal antibody against Syntaxin 6 offers a good possibility for IF imaging of the Golgi complex. It should be emphasized that it will be located mostly in the trans-Golgi network [67].

1.3 Conceptual formulation

The main aim of this work is to establish Raman micro-mapping as a method for noninvasive imaging on living cultured cells.

In consequence to the issues described above, we decided to perform the experiments in this work with a laser in the range of visible light (green, 532 nm). After it has been demonstrated that it was possible to visualize single organelles (mitochondria) on an ultrastructural level [63], it should be investigated if Raman spectroscopy allows a comprehensive delineation of the cell's biochemistry. Therefore, we focused on a group of organelles which form the main portion of the intracellular matter and also contribute to the high turnover of tumor cells. The compartments chosen were the nucleus, the endoplasmic reticulum, the Golgi apparatus, mitochondria and part of the filamentous scaffold, i.e. the microfilaments and thin filaments. As it is the gold standard method to depict these intracellular compartments, we performed immunofluorescence (IF) microscopy successive to Raman spectroscopy on the same cells. After both imaging methods had been carried out, the image pairs underwent a one-to-one registration. Different mathematical analyses, including the investigation for spectral patterns for each considered organelle, were used for extracting information on the subcellular compartments from Raman spectra. They aimed towards the construction of "artificial" IF-images (aIF images). Finding the correlation between both image modalities should examine the practical use of Raman spectroscopy as an imaging technique.

2 Materials and methods

This section presents the experimental setup used in this work. A detailed listing of the materials mentioned here and the corresponding manufacturers is provided in appendix B.

2.1 Cell culture

The cells used for all experiments in this work are of a human malignant glioma cell line, LN-18[1] (courtesy of Prof. Dr. van Meir, Lausanne). LN-18 cells show a bipolar or stellate shape, characterized by numerous microfilaments and an irregular cell surface with numerous microvili. They do not synthesize glial fibrillary acid or S-100 proteins, but large quantities of cytoplasmic fibronectin. Nuclei are plemomorphic and contain between 70 and 80 chromosomes (modal number 78, XXYY). The doubling time of LN-18 cells is approx. 72h at a plating efficiency of about 3% [26].

To allow a quantiative comparison between both imaging modalities, it had to be ensured that the very same cells were mapped with Raman microspectroscopy and IF microscopy. To facilitate an exact localization of a single cell, the cells were seeded on structured object slides, named England Finders. Figure 2.1 shows a detail of the grid on these slides. The grid is visible in the light microscopic setup of the Raman microscope as well as in the microscopic setup used for IF image acquisition.

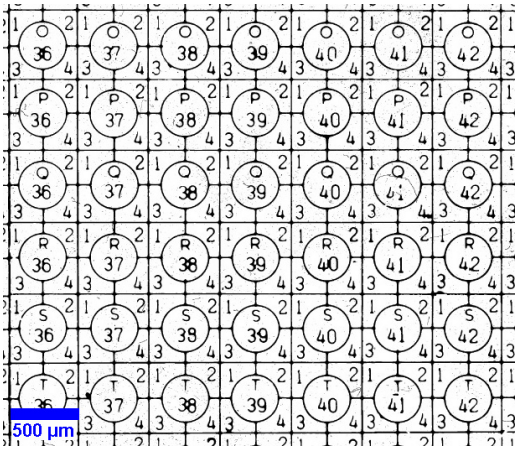

Figure 2.1: *England Finder. A fine grating provides full orientation over the whole object slide. [76]*

LN-18 cells were grown on England Finders in Quadriperm culture flasks under standard cell culture conditions (37° C, humidified

[1] ATCC number CRL-2610

atmosphere with 5% CO_2) in 6 ml Dulbecco's modified Eagle's medium (DMEM) supplemented with 10% fetal calf serum, 100 U/ml penicillin, 100 µg/ml streptomycin, and 2 mMol/ml glutamine. Incubation time was adapted to the cell growth to achieve a non-confluent monolayer of cells on the slides. After 48 – 72h of incubation, the England Finders were washed in phosphate buffered saline (PBS) at 37° C to remove all DMEM residuals before Raman measurements. Due to its coloring, DMEM causes a strong background signal which would superimpose the much weaker Raman signature of the biological sample. Thus, for measuring it has been replaced by PBS[2].

2.2 Raman microspectroscopical mapping

2.2.1 Raman system

All Raman measurements were carried out with an alpha300R confocal Raman microscope manufactured by WITec GmbH [106]. The setup was installed at the Department of Earth and Environmental Sciences, Ludwig-Maximilians-Universität, Munich, Germany. The setup of this microscope is described in chapter 1.1.3. Coupled to the microscope there are two other main components in the Raman setup. First, the second harmonic generation (SHG, 532 nm, frequency doubled) of a neodymium-doped yttrium aluminium garnet (Nd:YAG) single mode laser (1064 nm) is guided with a single mode fiber to the microscope, with a maximum laser power of 22,5 mW in front of the objective. Second, a lens-based spectrometer with a CCD camera is connected to the microscope via a multimode fiber. The optical resolution of the CCD-detector is 1024×128 pixel, Peltier cooled to -65° C.
The microscope setup remained unchanged throughout all measurements to ensure comparability and reproducibility. With a 60x water immersion microscope objective (working distance 2.0 mm, numerical aperture (NA) 1.0) an optical window of about 250×250 µm^2 is visible, and the cell(s) of interest can be centered manually in the field of view by micrometer screws. The sample itself can be moved with submicrometer precision on the piezo-driven scan stage during the scans, providing a 100x100x20 µm^3 movement. The recording time for single spectra was 70 to 80 ms, with a laser power adjusted to 10.0 mW, measured in front of the microscope objective. The 50 µm core of the multimode fiber leading to the spectrometer, as described above, acted as the pinhole for confocal imaging,

[2]Refer to appendix D.3 for average Raman spectrum of DMEM and appendix D.3 for average Raman spectrum of PBS.

resulting in a focal depth (resolution in z) of about 1 μm. The lateral resolution (x,y) is approx. 325 nm (for the 60x water immersion objective, NA 1.0), and limited by diffraction. The nominal spectral resolution, given by the 600 mm^{-1} grating of the spectrometer, was about 3.5 cm^{-1}.

2.2.2 Sample handling

The England Finder was clamped to an aluminium Petri dish and immersed in PBS at 37° C. LN-18 are relatively robust cells, which do not suffer when taken out of the nourishing medium for some hours. During the measurements, the cells remained in good condition, which was confirmed by repetitive inspection with light microscopy before and after each mapping.
From the light microscope video image, those cells which showed the typical widespread shape and seemed to be well attached to the slide were selected. The area to be scanned was exactly determined with help of the light microscope. Since the cells are adherent to the glass substrate, which may also contribute to the measured spectra, a x,z-map (depth scan) was acquired prior to mapping. The x,z-maps and the position of the nucleus, which can be easily detected by applying an integral spectral filter[3], helped in evaluating the measuring distance above the slide for the x,y-maps. The demand on the z-distance was, to offer both a high contribution from the sample, and a low contribution from the glass substrate to the Raman spectra.
After these preparatory scans, settings for the x,y-scans were defined. The distance above the substrate was typically set to about $z = 2\mu m$. The spatial resolution for the spectral recording was between 0.5 and 0.25 per μm. Then, the sample was raster scanned, with usual measurement times of approx. 45 - 60 minutes. A maximum of two recordings per object slide was performed, to keep the overall measuring time at a maximum of 3 - 3.5 hours (typically even shorter).
Directly after the measurements, light microcope images were acquired to check the cells' condition, the slides were washed in PBS and then fixed in 4% phosphate buffered formalin solution at room temperature. After fixation, the slides were washed again in PBS, and stored at 4° C.
To rule out potential artifacts through shrinking or distortion of the fixed cells, in comparison to the living ones, the identical cells were scanned again after fixation in several measurements. Here as well, after acquisition of Raman data the slides were washed and stored in PBS at 4° C.

[3] Material illustrating how images are generated by integration of selected spetral ranges is provided in appendix D.1.

The exact protocols for handling of the cells and Raman sampling are provided in the appendix, section C.1 and C.2.

2.3 Immunofluorescence staining and imaging

The cells were transported to the laboratories of the Division of Neuropathology, where staining was performed. After fixation in formalin and washing in PBS, cells were incubated with the primary antibody overnight at 4° C, and subsequently with the secondary antibodies conjugated to FITC, and with rhodamin-conjugated Phalloidin. Last, nuclei were stained with 4,6-diamidino-2-phenylindole (DAPI, Hoechst dye). Refer to appendix C.3 for dilutions and staining times.
Throughout all cells previously investigated by Raman spectroscopy, the cytoskeleton (red) and nucleus (blue) were stained and imaged. FITC was coupled to three different antibodies to additionally visualize the following intracellular compartments: mitochondria (anti-COX-IV Ab), the endoplasmic reticulum (anti-Calnexin Ab) and the Golgi apparatus (anti-Syntaxin-6 Ab).

The triple-stained samples were imaged using a Zeiss AxioImager microscope with standard software (AxioVision 4.5) and standard filter sets. For identification of the previously imaged Raman scans, the respective coordinates on the England Finder were identified with the fluorescence microscope. In addition, light microscope images of the cells before and after Raman sampling and images constructed with spectral filters from the Raman datasets were compared to the morphology of the same cells in the immunofluorescence images. To enable an optimal matching of the fluorescence images with the respective Raman data, in most cases a stack of 8 - 16 images per cell was acquired. The z-feed was 0.5 μm, with an average cell height (in z) of approx. 5 - 6 μm.

2.4 Data analysis

Preparation, registration and decomposition of the data has been carried out primarily at the Max-Planck-Institute for Extraterrestrial Physics, Garching, Germany [49].

Prior to this work, different experiments have been performed using Raman microspectroscopy to achieve imaging of subcellular structures. They are described in detail in section 1.1.4. Due to the high resolution reached by new Raman systems, even very small organelles such as mitochondria [63] or lipid bodies [64] could be visualized. Still, a full

biochemical interpretation, considering the different possible subcellular structures of a Raman hyperspectral dataset for a single cell is not yet feasible. This might be due to both composition of those compartments and the complexity of the information given in the Raman spectra. Except for the nucleus, that consists to a major part of nucleic acids and can be easily determined in a Raman microspectroscopic image, most of the extranuclear organelles contain lipids and proteins and, to a smaller amount, sugars or other carbohydrates. When the biochemical composition of compartments is relatively similar, it becomes difficult to extract specific properties of the compartments since spectral features are expected to overlap. Therefore, the approach of looking for specific spectral bonds, as performed e.g. in [77], has been disregarded. A new approach was chosen instead, which relies on pattern recognition in the spectra.

The primary aim of data analysis was the identification of cellular components in the Raman spectral maps, using only spectral characteristics and, thus, avoiding labeling procedures. For this purpose, in a training procedure, Raman maps and IF images were compared and specific Raman spectral signatures for each cellular compartment imaged in IF microscopy were obtained. In the following, the technique was applied to Raman maps without previous comparison to IF images, and only compared after construction of an ”artificial“ (Raman-based) IF image (aIF), according to its specific signatures. From the very extensive information contained in a Raman spectral dataset, only the part corresponding to the compartments under investigation in fluorescence microscopy has been exploited. Such, it is displaying characteristics, which assign the compartments to a group of spectral bonds, not to a single peak.

2.4.1 Data preparation

In a Raman dataset, each image coordinate ("pixel“) is associated with one spectrum. In our case, the spectra include the range of 0 - 3750 cm^{-1}. Before further use of the spectral data, the CCD dark counts were cleared by a spectral minimum subtraction. Cosmic rays, which occur due to relatively long integration times, and artifacts along the scan direction were eliminated by an anisotropic kernel filtering. After this, further random noise was reduced and other kinds of artifacts and pollution could be removed by a principal component analysis (PCA). Since after these steps of data preparation certain artifacts remained, which prevailed as horizontal lines, i.e. along the scan direction, an additional structure filter was applied.
Slight variations between measurements cause noise in the data. This uncertainty cannot be analytically tracked down to its source, since the experimental setup could not exactly

be reproduced in all measurement parameters. Thus, PCA components without structural content have been eliminated using a structural filter, which enhanced image quality. According to their anisotropic structural content, the principal components were rank ordered by an information based procedure. Finally, the first ten rank selected PCA components were transformed back. The resulting Raman images showed to be considerably improved with respect to the signal-to-noise ratio.

Figure 2.2 shows the primary PCA-components (upper row) in comparison to the PCA components after rank ordering. Note the systematic errors in the rejected panels (6, 7, 8, 10).

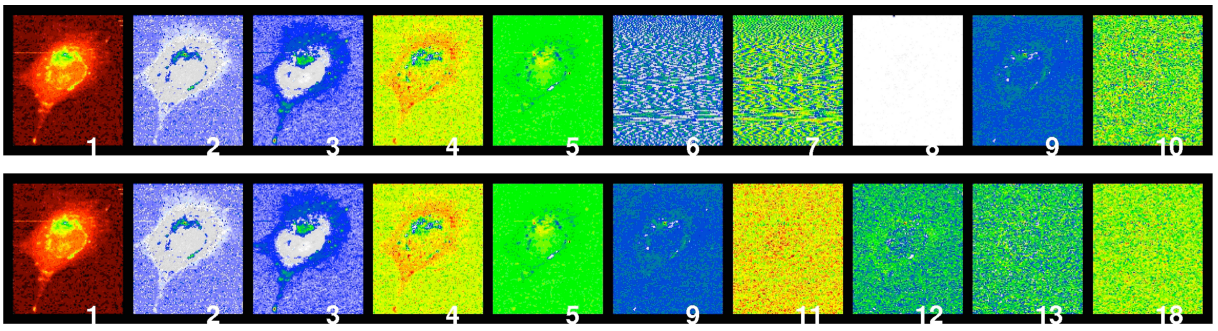

Figure 2.2: *Principal component analysis:*
Structural filtering of the principal components of a Raman spectroscopic image [49].
upper row *usual rank order of the components*
lower row *re-ordered components with respect to their anisotropic structural information content; note that components 1 through 5 remain in their original order, while components 6,7, and 8 were eliminated because of their high rate of artificial structural elements (systematic errors)*

2.4.2 Registration

Registration is necessary to optimize matching between the two image modalities. The registration procedure enables a pixel-to-pixel comparison of both image modalities. Among various different statistical measures, the approach relying on the concept of mutual information proved most suitable, since Raman and IF images differ in many ways. Due to the experimental setups and imaging protocol, neither nonlinear distortions nor rotations did occur. Thus, only linear transformations, which are global scaling (magnification) and translation (spatial offset) had to be considered.
During IF image acquisition (see chapter 2.3) multi section IF image stacks have been recorded. The registration procedure has been performed for each z-level seperately, and the best solution has been chosen.

2.4.3 Decomposition of Raman data

Data preparation and registration resulted in an optimal matching of IF images and the Raman spectral data, so that each color pixel of the IF image has a counterpart in terms of a Raman spectrum. The task was, to find a method to extract Raman spectral signatures of the cellular compartments identified by IF imaging. On the basis of the spectral signatures, aIF images can be constructed.

To do so, a method based on a redundancy analysis of both data modalities has been developed. To avoid overfitting, only a small number of relevant wavenumbers was selected. This means, this set of wavenumbers maximizes the redundant information between both image modalities. Refer to [49] for detailed mathematical explanation.

The considered wavenumbers were systematically selected by a method based on information theoretical principles. This methodological approach ends up with a set of spectral lines, which contains most information in direct correspondence to the respective IF image layer. In the end, this set of wavenumbers is utilized for the construction of aIF images. As the representative set of wavenumbers was found for a certain intracellular compartment of interest, the Raman subspace was fitted to the respective IF image layer.

The fitting procedure results in a specific set of fit parameters for each IF channel (RGB as: red - cytoskeleton; green - 1. endoplasmic reticulum, 2. mitochondria, 3. Golgi apparatus; blue - nucleus). Note that the spectral regions of high information content, which contribute strongly to the polynomial fitting from Raman subspace to IF, are not always correlated to wavelengths with obvious Raman peaks. Therefore, not only the spectral regions called the biochemical "fingerprint“ of the sample contribute to the construction of aIF images, but the simultaneous information given by a whole set of spectral wavenumbers specific for each respective organelle, illustrated as barcodes (see Fig. 3.5).

Finally, for each respective organelle, an aIF image based on Raman data was constructed. These aIF images were compared to the actual fluorescence image channels. The accuracy between aIF and IF images was assessed by Pearson’s coefficient of correlation ρ for each image channel seperately.

3 Results

3.1 Experimental results

Single living cells of the human glioblastoma cell line LN-18 have been investigated by laser scanning microscopy in combination with Raman spectroscopy. The experiment ran with minimal scanning times and laser power, to save the living specimen while maintaining a suitable spectral quality (see section 2.2). The lifetime of LN-18 cells is known to be significantly longer than the measuring timescale. Accordingly, the cells under investigation were expected to be unaltered during data acquisition. Light microscope controls before and after exposition to the laser were carried out to validate shape and viability of the single cells. Light micrographs were also compared to images constructed by spectral filtering[1] from the Raman datasets to confirm similarity in shape and size. With this setup and set of parameters, it was possible to measure living cells with a laser in the range of visible light (532 nm) in PBS immersion (with reservoir to keep 37° C) with an integration time of approx. 70 ms per pixel, which resulted in a recording time of approx. 45 - 60 minutes for one measurement.

To rule out strong, superimposed signals from the glass substrate, a depth scan (x,z) was carried out for every run prior to horizontal (x,y) mapping. The distance to the substrate was chosen to achieve a minimum contribution of the glass substrate to the Raman spectra. An average spectrum of the glass slides[2] used in these experiments served as an object of comparison. Figure 3.1 illustrates the selection steps for the z-scan and the x,y-scanning frame (panel 1, red). Panel 2b shows the x,z-scan, which helps to define scanning height (panel 2a). The x,y-scan resulted in a high resolution Raman map, in which every "pixel“ consists of one spectrum in the range of 0 - 3750 cm^{-1}. Autofluorescence was not observed in any measurement on LN-18 cells. After Raman data was obtained for one scanning field, the cells were fixed in formalin and stored in PBS until immunofluorescence dying and imaging could be carried out.

[1] Material illustrating how images are generated by integration of selected spetral ranges is provided in appendix D.1.

[2] Data provided in appendix D.3.

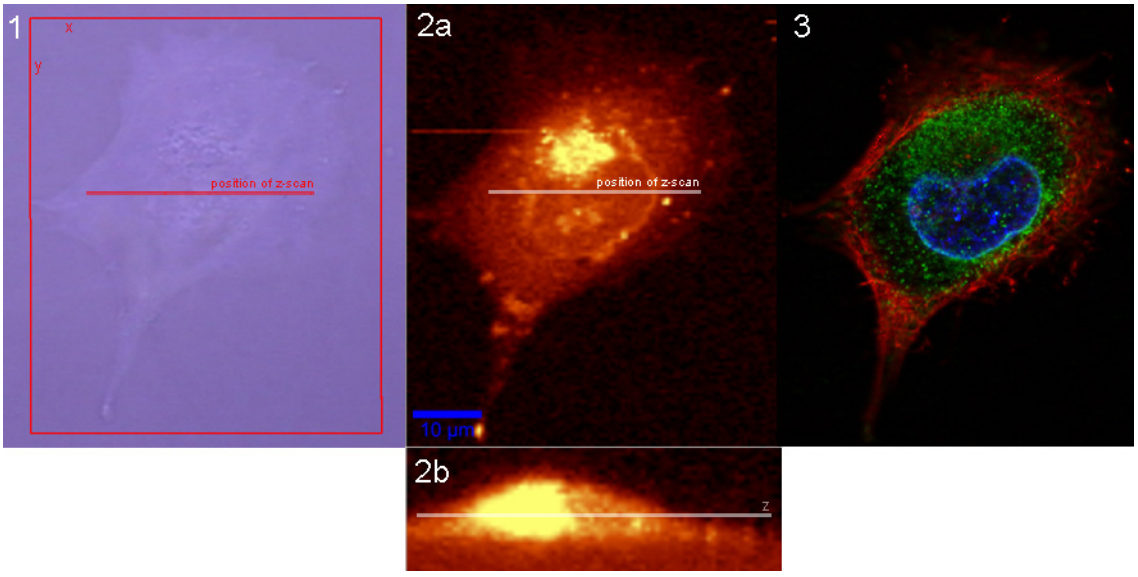

Figure 3.1: *Experimental sequence:*
After recording a light micrograph, a x,z-scan was performed to determine z-height (panel 2b) for the x,y-scan (panel 2a). Panel 3 shows the respective IF image as a first, visual, comparison.

1) light micrograph: living LN-18 cell; red lines: scanning frames for x,y Raman mapping and scanning position for z-scan

2a) Raman x,y-scan, living sample cell, intensities integrated over 2800 – 3050 cm^{-1}

2b) Raman x,z-scan, living sample cell, intensities integrated over 2800 – 3050 cm^{-1}

3) combined three-channel fluorescence image (rhodamin: phalloidin / FITC: anti-Calnexin / DAPI)

Since the experiment aimed at the construction of aIF images from spectroscopic data, two variables had to be considered. First, during the calculation of spectral patterns from the two image modalities, the position of intracellular organelles must have remained constant in Raman data and IF images. Second, the cell's shape and spectral characteristics must not have changed significantly due to fixation. To respect these factors, Raman datasets from living as well as from fixed cells were included in the training datasets. Figure 3.2 opposes the Raman-based aIF images of both the living (panel a) and the fixed cell (panel c) to the corresponding IF image (panel b). Further material on cellular shaping before and after fixation is provided in appendix D.2.

Immunofluorescence imaging is the gold standard method to depict subcellular structures or to specifically target intracellular processes. In this work, it has been used subsequent to Raman mapping on the same specimens to enable a direct comparison with the Raman datasets.
In all samples, rhodamin-conjugated phalloidin served as an indicator for the outer margins of the cells. It specifically binds to actin structures, which form a major part of the cell's framework. Just as well, throughout all samples, the nucleus as the most prominent

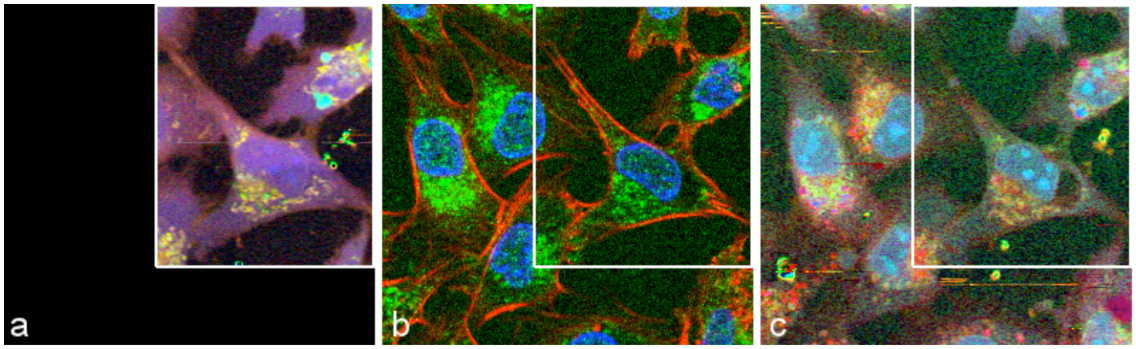

Figure 3.2: *Comparison of aIF images of native and fixed cells with the corresponding IF image. The very same cells have been measured with Raman spectroscopy before and after fixation. Immunofluorescence staining and imaging has been conducted subsequent to both Raman scans.*
In all panels, the green channel depicts the Golgi apparatus. Note that the overall shape of the cells (cytoskeleton, nucleus, and even nucleoli) is preserved throughout both aIF images. The disbribution of the Golgi system does not change significantly. Still, the central cell is affected by a fixation artifact (panel b and c). The frames in the panels indicate the common parts of the images, since the Raman recording in panel a covers a smaller section as panel b and c.

a) Raman-based aIF image of a living LN-18 cell
b) IF image of the same cell after fixation (rhodamin: phalloidin / FITC: anti-Syntaxin-6 / DAPI)
c) Raman-based aIF image of the same cell after fixation [49]

intracellular structure has been stained with DAPI.
The green channel represents different structures. Three organelles have been chosen to be depicted, namely the mitochondria, the endoplasmic reticulum, and the Golgi complex. The latter two are important for the biosynthesis and modification of proteins and lipids, and as such contribute to the major substance of the cell, while mitochondria supply the cell with energy. All three are important components regarding fast cell replication, as seen in tumor cells. Specific antibodies against membrane elements in these organelles have been chosen and were secondarily conjugated to FITC: anti-Calnexin Ab, an antibody against a chaperone positioned in the membranes of the endoplasmic reticulum, anti-COX-IV Ab, an antibody against an integral membrane protein of the inner mitochondrial membrane, and anti-Syntaxin-6 Ab, an antibody against a SNARE protein located in the Golgi membranes.

The five regarded cellular compartments could clearly be identified in the fluorescence images. Panel 3 in figure 3.1 shows a LN-18 cell stained with phalloidin, DAPI and FITC-conjugated anti-Calnexin Ab. The stellate shape and the prominent nucleus are typical for this cell line. Phalloidin clearly indicates the cellular borders. Actin components can be observed throughout the whole cell, but show higher density in the periphery. The nucleus

binds its fluorescent marker inhomogeneously, which is consistent with its pleomorphic shape, showing usually more than one nucleolus. The endoplasmic reticulum spreads out loosely and evenly throughout the cytoplasm.

Figure 3.3 illustrates the spatial spreading of the mitochondria and the Golgi sheets, as observed on glioblastoma cells by fluorescence imaging.
LN-18 are highly proliferative cells. Such cells are known to express high numbers of mitochondria, which make a significant part of the intracellular structures. As expected, mitochondria show a distinct and strong signal. They can show different shapes: in certain cases they are located rather peripherically, in others (figure 3.3, panel 1), they build tubular networks which can also appear in vicinity of the nucleus. The Golgi cisterns prevail in the perinuclear space (figure 3.3, panel 2). Thus, the perinuclear regions are most likely to contain components of several of these intracellular compartments. The actin filaments are spanned through these regions, in which Golgi sheets are stacked into, or next to, the layers of the endoplasmic reticulum.

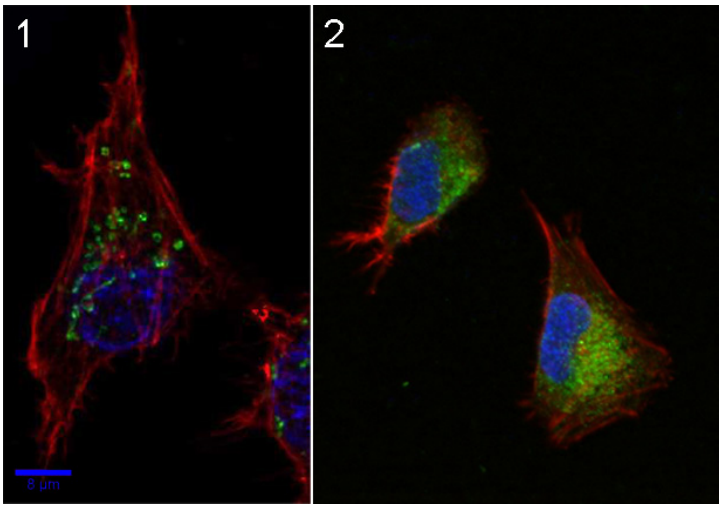

Figure 3.3: *Immunofluorescence images: Organelle distribution in LN-18 cells*
1) Rhodamin: Phalloidin / FITC: anti-COX-IV Ab / DAPI
2) Rhodamin: Phalloidin / FITC: anti-Syntaxin-6 Ab / DAPI

3.2 Discovering Raman characteristics: Label-free imaging

By following the defined measurement protocol, it was possible to register both image modalities exactly, adjusting magnification and spatial offset only. Distortions or rotations have not been observed. Thus, a combination of datasets of different origin could be achieved, in which every color pixel on one form of image data have a corresponding counterpart in the other one.

Figure 3.4 shows a stepwise overlay of Raman and IF data, to visualize the quality of the data registration. The upper left panel shows only the spectrally integrated Raman data in a spectral range of 80 – 3040 cm^{-1}, the lower right panel only the three-channel

fluorescence picture. The round shaped object fluorescing blue in the upper right quadrant next to the cell is a fixation artifact, which is visible only in the fluorescence image and not in the Raman data.
On Raman data, a principal component analysis was performed. After rank ordering, the first three PCA components have been considered for registration.

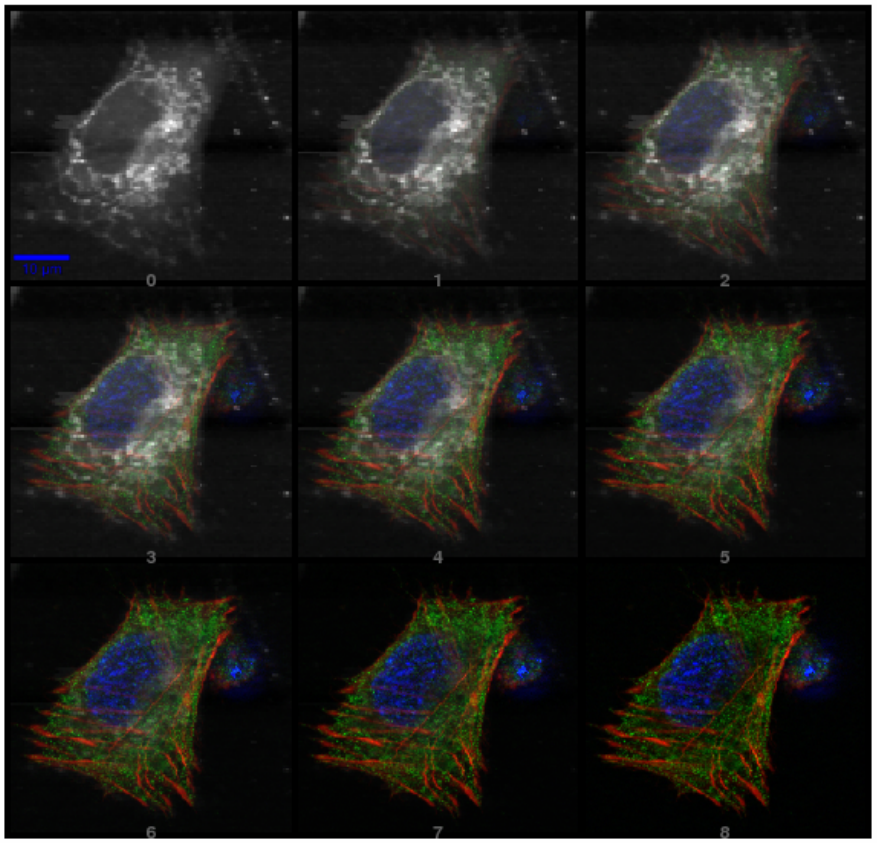

Figure 3.4: *Crossfade: Raman and IF images of the same cell, illustrating the registration of both image modalities.*
Upper left: integrated Raman data (80 – 3040 cm^{-1})
Lower right: IF image (Rhodamin: Phalloidin / FITC: anti-Calnexin Ab / DAPI)
The stepwise overlays demonstrate a reasonable image registration. For the registration procedure, the first n=3 (rank ordered) PCA components were considered.

After optimal matching of the image pairs, a methodology for decomposition of Raman spectral data has been applied. When directly matching pairs of corresponding images, there is an implicit risk of overfitting. This means, that specific relations in a pair of images are filtered out and overestimated, while their actual information content in relation to the biological problem might be of minor importance. To avoid this, a two-stage procedure has been applied. First, only a limited number of wavenumbers with the highest

information content for the respective intracellular compartment were selected. Second, a "leave-one-out“ technique was used for reconstruction. For each variable of the green color channel (anti-Calnexin Ab, anti-COX-IV Ab, anti-Syntaxin-6 Ab) multiple pairs of Raman datasets and IF images have been acquired. To construct an aIF image from one Raman dataset, which shows the same structures as its corresponding IF image, a training sample was generated out of all datasets except the one under consideration.

For the organelles of interest, representative sets of averaged spectra have been determined. The crucial information in Raman spectra, which allows a visual ”IF-like“ interpretation, is not determined by those average spectra, but by the wavenumbers with high spectral information mentioned above, visualized in terms of barcodes. Only the full set of fit parameters, given for each of the five categories of immunofluorescence stainings, allows a reasonable aIF construction. Figure 3.5 presents a set of representative average spectra for the cellular compartments investigated in this work: the cytoskeleton, the nucleus, the endoplasmatic reticulum, the mitochondria, and the Golgi apparatus. The background spectrum is given for comparison in figure 3.5a, the single spectra shown in figure 3.5b were calculated by subtraction of this background from the average spectrum of the indicated organelle. The prominent features of the background spectrum are due to the immersion medium (PBS)[3], giving a strong signal in the first 800 wavenumbers, a small peak at approx. 1600 cm^{-1}, as well as a rising shoulder in the region > 2800 cm^{-1}, and a minimal hump caused by the glass substrate at about 1100 cm^{-1}. Since these contributions might cause confusion or mislead in a biochemical interpretation of the spectra, they are eliminated by calculating the spectral differences shown in figure 3.5b.
Spectral regions of high information content are shown by the barcodes laid over every spectrum. Note that these areas of high information content might not only reflect positive spectral features, namely specific peaks, but also the absence of peaks, meaning peaks which occur everywhere else but here. Thus, the intensities of the chosen wavenumbers can contribute positively or negatively to the aIF image.

Spectral assignments are provided in appendix A. Many of the regions which contain high information on the intracellular compartments are localized in the very low wavenumbers (approx. 80 - 200 cm^{-1}) and in the high wavenumbers (>2800 cm^{-1}). For these areas, yet very little is known about specific assignments to chemical properties of the material. In the following, only those spectral areas are described which lie in the center region of the spectrum, and for which assignments are given in literature.
For the microfilaments and small filaments, areas of interest seen in the barcodes (figure 3.5, panel b, indicated red), are positioned at approx. 560 cm^{-1} (occuring e.g. in ade-

[3] Refer to appendix D.3 for average Raman spectrum of PBS. The Raman signature of PBS depends mostly on its water component.

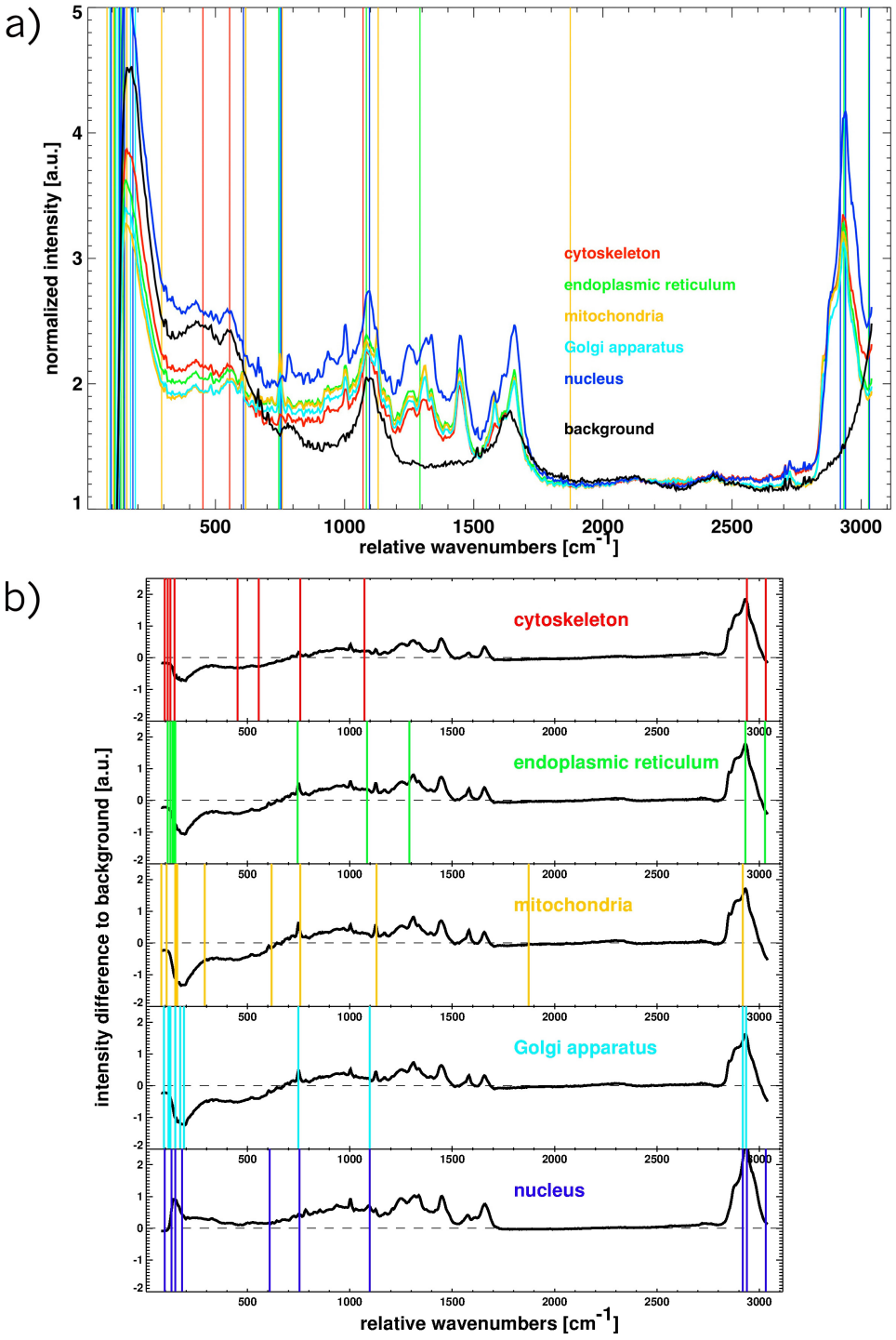

Figure 3.5: *Average spectra, displaying pectral characteristics of the five intracellular compartments. The overlaid barcodes indicate spectral regions of highest information content.*

a) Average spectra of each intracellular compartment and background [49]

b) Single compartments: difference between the average spectra shown in panel (a) and the background spectrum

nine, glycine [21]), at approx. 750 - 760 cm^{-1} (symmetric ring breathing mode of tryptophane[4]), and at approx. 1080 cm^{-1} (occuring e.g. in oleic acid and trehalose [21]).
Barcodes descriptive for the endoplasmic reticulum consist of wavenumbers at 750 cm^{-1}, 1090 cm^{-1}, and 1290 - 1295 cm^{-1} (figure 3.5, panel b, indicated green). The first spectral line occurs e.g. in thymine and glutamate [21], the second one in serine, aiso acids, and the PO_2^- symmtric stretching mode of phosphate esters[5], and the third spectral line in different fatty acids [21].
For mitochondria, four spectral lines located in the center of the spectrum can be identified (see figure 3.5, panel b, indicated yellow). The lines which are described in literature are at approx. 610 - 620 cm^{-1} (found e.g. in thymine, serine, and arginine), at approx. 770 cm^{-1} (found in different amino acids, e.g. in alanine, valine, glutamate, tryptophane, proline, fatty acids, sugars, and glutathione), and at approx. 1120- -1230 cm^{-1} (as it occurs e.g. in different sugars and succinic acid) [21].
The Golgi apparatus corresponds to two spectral lines in the central range (see figure 3.5, panel b, indicated turquoise). The first one is at approx. 730 cm^{-1}, a line which occurs e.g. in alanine, tryptophane, and trehalose [21]. The second line is at approx. 1100 cm^{-1}. It can be assigned to the PO_2^- symmetric stretching mode of phosphate esters [6]. This spectral line is adjacent to one defining the endoplasmic reticulum, although there is no overlapping. The same line is also neighboring to one of the lines characteristic for the nucleus, here an overlap is observed. All other regions of high specific information for pixels conforming to the Golgi system are located either in the range of very low wavenumbers or in the peaks given by CH-stretching modes (CH_3, CH_2, CH; wavenumbers > 2800 cm^{-1}).
For the nuclei, the only spectral regions for which biochemical information is provided, are the three central lines (figure 3.5, panel (b), indicated blue). The first two are at approx. 605 - 610 cm^{-1} (occuring e.g. in glycine, phenylalanine, glutamate, and different sugars) and at approx. 750 - 760 cm^{-1} (found e.g. in the symmetric ring breathing in tryptophane) [21]. The latter one is also present in the barcode of the microfilaments (figure 3.5, panel b, indicated red). The remaining spectral line is at approx. 1100 cm^{-1}. As mentioned before, this line gives information on a content of PO_2^- symmetric stretching modes of phosphate esters and can be identified also in the barcode representative for the Golgi system.

The average spectra for the endoplasmic reticulum, mitochondria, and the Golgi apparatus, as illustrated in figure 3.5, seem to be similar to each other on the first view. To the average spectra of the nucleus and the cytoskeleton, clear differences can be identified by visual inspection. The spectral differences between the average spectra of the ER, mitochondria,

[4] cf. appendix A
[5] cf. appendix A
[6] cf. appendix A

and the Golgi apparatus are shown in figure 3.6. Here, the common and divergent spectral characteristics between those compartments can be clearly observed.

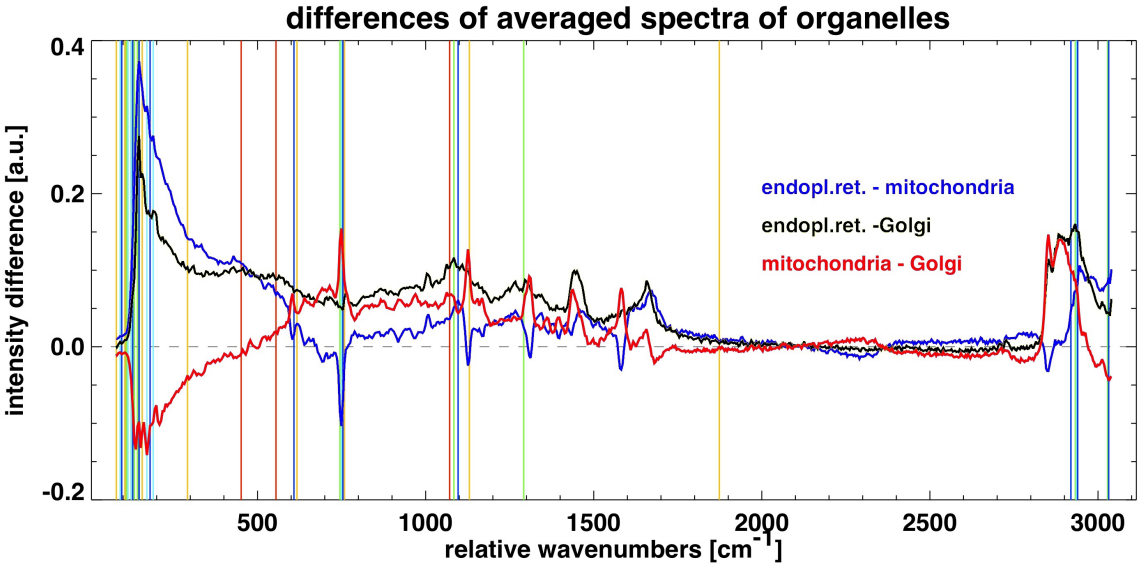

Figure 3.6: *Difference spectra between different average spectra displayed in figure 3.5. The barcodes corresponding to the organelles are indicated in the color assignment given in figure 3.5. [49]*

Processing the full set of parameters allows construction of aIF images from Raman data, which depict information similar to that of the fluorescence images. The accuracy of these constructed aIF images is indicated by the correlation coefficient between the images from different sources.

Figure 3.7 shows the single-channel as well as the overlaid three-channel IF original (upper row) and the corresponding Raman data, processed as aIF images (lower row). A first visual screening already gives an impression on congruence of the single color channels. The channels are chosen according to the fluorophore colors in the IF image. The red channel shows the cytoskeleton, the green channel, in this case, the Golgi system, and the blue channel the nuclei of the cells.

In the first channel (the cytoskeleton, figure 3.7, panel a for IF, and e for Raman data), the largest divergence between both methods is observed. While phalloidin specifically binds to actin polymers and indicates strong microfilament bundles, the actin signal in the Raman spectra is observed consistently throughout most of the cytoplasm, exept for the nucleus and the background. The shapes of the cells can clearly be determined, whereas the alignment of the single bundles can hardly be reproduced. Since the colocalization of the signals is variable, the correlation coefficient is low ($\rho = 0.36$).

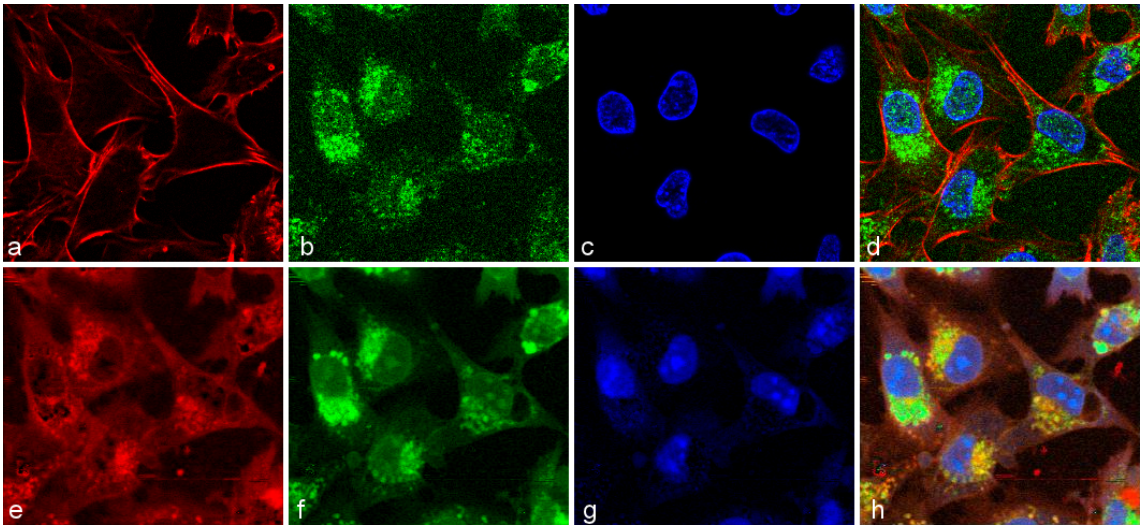

Figure 3.7: *IF image and Raman-based aIF images.*
a – d: *immunofluorescence image of LN-18 cell.*
a: *Rhodamin: Phalloidin*
b: *FITC: anti-Syntaxin-6 Ab*
c: *DAPI*
d: *three-channel IF overlay*
e – h: *aIF channels constructed from the Raman dataset obtained from the same cell*
h: *overlay of the three aIF channels [49]*

The green channel, displaying the Golgi apparatus in the IF image (panel b), shows a better congruence. Raman signals found in the Golgi apparatus are present, in lower intensities, throughout most of the cells body, while condensing in the regions clearly indicated in the IF picture to belong to this organell. The correlation between both images (green channel) is $\rho = 0.71$.
The correspondence of both image modalities seems to be most reliable in the blue channel (panel c for IF, and g for Raman data). The position of the nuclei can clearly be defined. The IF image (panel c) reveals central areas with lesser intensities. The aIF images, in contrast, show a strong signal in these areas, which can be correlated to a signal given by RNA or by proteins found in the nucleolus. The clear identification of nuclei by Raman microspectroscopic image is confirmed by the correlation coefficient of $\rho = 0.74$.
In the three-channel overlay (panel h), the three-channel IF image (panel d) is artificially constructed with Raman data. The correlation coefficient between the RGB aIF image and its RGB IF counterpart is $\rho = 0.6$. It should be noted that, unlike the IF image, the Raman data allows to generate images with more than the three channels displayed at once. In the experimental setup described in this work, five subcellular structures were visualized, namely, the nucleus, the cytoskeleton, the endoplasmic reticulum, mitochondria, and the Golgi apparatus. Out of any Raman spectral map, an image can be computed,

which is displaying all five structures included in the training pool. The accuracy of the reconstructions in correlation to the corresponding fluorescence channels is indicated by the respective correlation coefficient. For 21 measurements (all channels), the mean correlation coefficient $\bar{\rho}$ is 0.593 for the endoplasmic reticulum (standard deviation 0.273), and 0.60 for mitochondria (standard deviation 0.122)[7].

For any compartment, a number of scans and corresponding IF measurements have been carried out. This way, the algorithm could be trained on different samples. Images which show more than one single cell, as e.g. figure 3.7, give a first impression on the precision of the method. The features described above can be detected in all cells in the field of view.

Figure 3.8 shows a set of images generated from Raman data (column 2 to 4), which are depicting all five organelles imaged in fluorescence microscopy. In each image, the red color channel shows the cytoskeleton and the blue color channel the nucleus, the same applies to the fluorescence images given in column 5. As for the constructed aIF images, column 2 shows the endoplasmic reticulum in the green channel, column 3 the mitochondria and column 4 the Golgi apparatus. The leftmost column gives an impression of "raw“ Raman data, i.e. Raman data integrated from 80 - 3040 cm^{-1}. Hence, this panel is depicting the cells not very sharply. The corresponding aIF image of the cell is found as follows: the analog aIF image for A5 is A2, the one for B5 is B3, and the one for C5 is C4. For each pair given above, the remaining two panels in the respective row show the organelles which have not been stained in that cell. Note, that for generating the corresponding aIF image, the one under consideration is removed from the training sample (following a "leave-one-out“ procedure).
The first impression of these pictures is, that a three-channel aIF image is much more blurred than the corresponding fluorescence image. This is mainly given by the nature of the methods (cf. section 4). The intensities for the blue channel are almost exclusively restricted to the area, in which the nucleus is actually shown in the fluorescence image. The red signal occurs in most cells throughout the whole cytoplasm but the nucleus, and shows higher intensities towards the periphery, as e.g. given in panel A3. Note that, in row C, the ”red“ Raman channel shows the cellular shape and the outer limits of the central cell even better than the fluorescence image[8].
In the green channel, on the other hand, evidently higher intensities assemble in the perinuclear area for all three organelles shown in column 2 to 4. Differences between the three

[7] Cf. to appendix D.4 for all measurement statistics

[8] Z-offset as a reason for non-concordance between both imaging modalities could be excluded through registration techniques using a whole z-stack of fluorescence images. Refer to chapter 2.4.2 for detailed explanation.

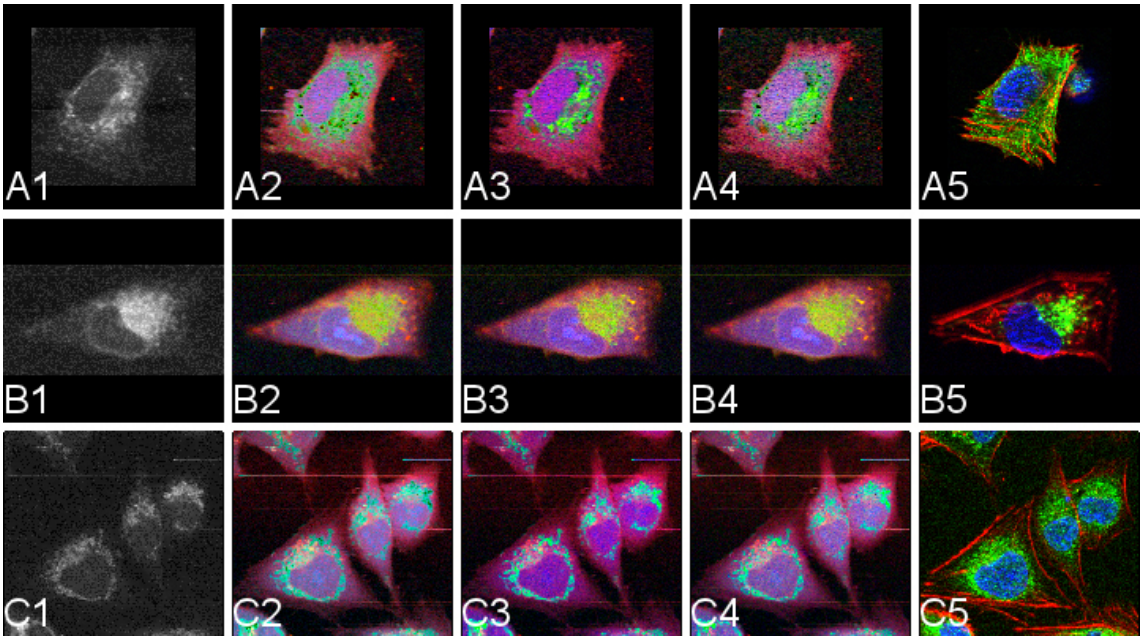

Figure 3.8: *Three-channel reconstructions from Raman data.*
From left to right: Raman raw data, constructed Raman-based aIF images and original IF images of LN-18 cells of all three variables of the green color channel.

column (1)	*Raman data, integrated over the full spectrum (80 - 3040 cm^{-1})*
column (2)	*Reconstruction showing the endoplasmic reticulum in the green channel*
column (3)	*Reconstruction showing mitochondria in the green channel*
column (4)	*Reconstruction showing the Golgi system in the green channel*
column (5)	*Immunofluorescence images, as follows:*
(A5):	*Rhodamin: Phalloidin / FITC: anti-Calnexin Ab / DAPI (green: ER)*
(B5)	*Rhodamin: Phalloidin / FITC: anti-COX-IV Ab / DAPI (green: mitochondria)*
(C5)	*Rhodamin: Phalloidin / FITC: anti-Syntaxin-6 Ab / DAPI (green: Golgi complex)*

Among the aIF channels, compare panel A2, B3, and C4 with the respective RGB IF image in the rightmost column 5 [49].

green channels are to be seen only at a closer view. The yellow-green shading showing the endoplasmic reticulum in panel A2 reaches almost fully into the periphery of the cell, while in panel A3 it is restricted to the central areas.
In row B, differences between the perinuclar green intensities in column 2 to 4 seem to be indistinct on the first view. The intensities showing mitochondrial distribution (figure 3.8, panel B3) are localized similar to those representing the Golgi system (panel B4). The endoplasmic reticulum, however, reaches further into the periphery of the cell (panel B2). The arrangement of mitochondria is in correspondaence to the fluorescence image (panel B5), which shows a strong signal in the perinuclear region, while there is almost no signal in the periphery for that respective z-layer.

The Golgi complex seems to be depicted well by the aIF image. Figure 3.8, panel C4 clearly shows green intensities, which are corresponding to the Golgi signal in the IF image. The signal fades towards the periphery of the cell. Mitochondria (panel C3) localize in similar regions, but have a rather distinct shape. Sheets of the endoplasmic reticulum can be located between the Golgi membranes, but spread out farther than the Golgi sheets (figure 3.8, panel C2).

4 Discussion

Raman spectroscopy offers a new approach for noninvasive imaging on living cells. It has been adapted for use on biological material in interdisciplinary studies, which range from investigations of purified biological molecules [21], different tissues [14, 73], and experiments on living cultured cells [16], to in vivo applications on patients [8]. However, for investigations on single cells on an ultrastructural level, the method has not yet been fully refined [16, 63]. The aim of this experimental approach was to fathom the practicability of Raman spectroscopic raster scanning as a method for noninvasive and label free imaging of subcellular structures on living cells by image construction based on Raman data.

In the present work, single living glioblastoma cells have been investigated under a Raman spectroscopical setup with a laser in the range of visible light. The method was performed completely label free and the cells did not show any laser induced damage. Subsequent to Raman spectroscopy, immunofluorescence microscopy has been performed on the very same cells, depicting a selection of cellular organelles. A direct comparison of the two image modalities was enabled by a one-to-one overlay. With help of the IF images, it was possible to calculate spectral patterns (barcodes) for the chosen subcellular structures, i.e. the nucleus, the cytoskeleton, the endoplasmic reticulum, mitochondria, and the Golgi apparatus. It could be clearly shown that the constructed high resolution Raman-based ”artificial“ IF images (aIF) depict the chosen organelles well. The correlation coefficient between both imaging modalities reaches up to ρ=0.74.

Raman (micro-)spectroscopy and fluorescence imaging are two complementary methods. In Raman spectroscopy, inelastically scattered light from a given focal area (in our case, an (x,y,z)-voxel of approx. $325 \times 325 \times 1000$ nm^3) can be detected. Modern microspectroscopy setups allow a high quality raster scanning of samples as well as a detailed spectral interpretation with a very short integration time per point. The Raman measurements result in a dataset of one Raman spectrum (0 - 3750 cm^{-1}) for each point scanned. Each spectrum contains broad information on the biochemical content of the material and can be interpreted in many different aspects. The material composition can be evaluted by interpreting the Raman peaks in terms of functional groups. When the goal is an examination of the subcellular structures of single cells by their biochemical composition, vague

estimations of the position of cellular compartments can be stated by mere spectral analysis. For example, a high concentration of nucleic acids can be displayed by specific bonds in the region of the nucleus[1], while in regions outside the nucleus, bonds for proteins, lipids, and carbohydrates prevail. Finding average spectra for different purified substrates, intracellular components, or subcellular compartments allows more accurate assignments. Still, to receive purified material, cells must be handled destructively.
Here, a different interpretation approach is described, where spectral filtering not only for single peak identification or investigation of certain spectral regions (such as the "fingerprint region“), is performed, which would mean a focus on one chemical constituent. The investigations aim towards a spectral pattern specific for a certain combination of constituents. In our case, such a pattern, or set of spectroscopical features, shall be specific for one of the considered intracellular compartments. In principle, the spectral pattern is a complex of spectral features, which contain the information necessary to discriminate among the different cell compartments. Eventually, the spectral pattern may be resolved and interpreted by providing the biochemical meaning of every Raman peak.
Raman spectroscopy provides the investigator with a spectral map, which contains highly comprehensive information on chemical composition. It remains on the focus of the investigator and the methodological capabilities, in which direction the information provided by these spectra will be extracted and interpreted. The generation of images constructed out of spectral information is a reasonable approach: In bioanalytical and biomedical fields, evaluation of images is an everyday business, while the interpretation of spectra is usually not a routine procedure.

Fluorescence microscopy, on the other hand, is an efficient and highly specific imaging method. In bioanalytical fields it is the current gold standard method for visualization of intracellular compartments, and even dynamic processes. Typically, a selective antibody specifically binds to a certain intracellular component. It is linked to a fluorophore which can be visualized microscopically by its fluorescence. The use of exogenous markers, such as antibodies and fluorophores, might induce changes in the cell and alter the biochemical properties of the molecules [64]. For imaging, all visual information in the field of view but the fluorescing particles is suppressed by spectral filtering. Thus, a highly specific image displaying only the objects of interest (down to single molecules) ist generated. Still, only known molecules, for which specific antibodies are available, can be imaged. Immunofluorescence microscopy is an effective but limited method.
The specificity of immunofluorescence marking can be favorable, if the target molecule is known, but it is unfavorable, if a rather general approach is needed. For example, an antibody displaying "the Golgi system“, as the anti-Syntaxin-6 antibody used in this work,

[1] cf. appendix A

will always give a signal where the antibody-antigen reaction occurs, namely, in the Golgi system. Since Syntaxin 6 is mainly expressed in the trans-Golgi network [9], though, parts of the Golgi system (namely, the cis-Golgi network) might only be depicted inadequately. Therefore, the anti-Syntaxin-6 antibody, being only of limited suitability in this work, is still the best option available. Similar considerations apply to other samples.
Therefore, fluorescence microscopy is a specific method, which can be applied only if a certain a priori knowledge on the constitution of the specimen is present. It allows judgements only on the specific targeted molecule. This specificity is in contrast to the broad range of information obtained with Raman spectroscopy. While an antibody against an integral membrane protein of the Golgi apparatus specifically binds only where its antigen is located, the Raman spectra associated to the Golgi apparatus unvails the presence of different biomolecules (we would expect mainly proteins, lipids and some carbohydrates, to a lesser extent nucleic acids). Of course, most of those molecules will be found all around the cell, in different concentrations. Even the spectral pattern, which is the most specific feature derived for the cellular compartment, is by fare more vague than the fluorescence image.
This is best shown when focusing on the cytoskeleton (cf. figure 3.7, panel 1 and 5), since phalloidin strongly binds on filamentary actin, as actin appears in the formalin-fixed cell. Actin monomers are less likely to be depicted by phalloidin. Furthermore, phalloidin stabilizes actin towards the filamentary form [5]. The spectral pattern obtained by training on actin filaments reveals biochemical information on actin, which is not contained in other parts of the cell, or information which is *not* contained in actin but in the rest of the cell. Both ways, we receive information on actin, not only on its filamentary state. Therefore, the resulting aIF image of actin will always be more blurred than a fluorescence image of rhodamin-conjugated phalloidin bound to actin bundles.

In summary, an overlay of those two image methods could be achieved. However, some aspects concerning intrinsic factors of each technique have to be considered when evaluating the results. Here, immunofluorescence microscopy was chosen not because of its methodological closeness, but because it is the gold standard technique for visualization of intracellular processes.
Raman spectroscopy provides broad information of the sample which later on has to be filtered with a focus on the particular molecule, compartment, or any other feature of interest. The raw data itself does not reveal a large amount of self-evident information: extensive biochemical information exists in the spectra, but it may be hidden. Without further analysis, a clear interpretation is hardly possible. Fluorescence microscopy requires a priori knowledge and consideration about the target, thus revealing highly specific information, down to the molecular level. The images generated allow a direct interpretation,

without further need of processing. Raman spectroscopy needs no markers or dyes, and can be carried out on living cells. The information obtained depends on the biochemical composition of the sample. It can be carried out on living cells. Fluorescence microscopy demands staining, thus often requiring fixation and processing with different exogen materials. Raman spectroscopy is inefficient. Only when using an advanced microscopic technique, high quality spectral images can be achieved, which might eventually be suitable for quantitative analysis. Fluorescence microscopy, on the other hand, is highly sensitive. We compare a comprehensive method with a selective and sensitive one.

In this work, we observe localization of the cellular organelles mostly as expected, regarding the literature. In the following, the single compartments visualized shall be descriptively discussed.

LN-18 cells are known to contain numerous cytoplasmic microfilaments, which stabilize the motile cells and arrange mostly in the periphery, close to the cell surface [26]. As seen in figure 3.1, 3.3, 3.4, 3.7 (panel 1), and 3.8 (column 5), the line-like actin bundles branch throughout the whole cells, condensing towards the outer cellular limits [28]. Filamentary actin can be visualized clearly by phalloidin [5, 109], still it has to be expected that, through fixation and staining, the actin conformation of a cell will be shifted from monomers towards filamentary actin [20, 104]. Since phalloidin specifically binds on actin filaments, the actin monomers floating in the cytoplasm are not imaged, or only to a limited extent. In Raman reconstructions, this line-like appearance is not observed, which results in a relatively low correlation coefficient (for overall 21 measurements considered, the mean correlation coefficient $\bar{\rho}$ is 0.462, standard deviation 0.156)[2]. Given the intrinsic differences between the imaging methods, it can be assumed that the information obtained from areas with a high amount of filamentary actin, as used for training towards an 1:1 overlay, result in a barcode which is representative for actin in general, but not specific for filamentary actin. Therefore, the signal can be observed all through the cytoplasm of the cells (see 3.7, panel e), while sparing out regions where no actin should be observed at all, e.g., the nucleus, including nucleoli, and the extracellular space.
Furthermore, the intensity of the red channel (aIF image in Fig. 4.5 panel e) is systematically lowered for the pixels representing nucleoli. The spectral pattern for the cytoskeleton seems to be insensitive to the biochemical composition of nucleoli. This might be due to specific amino acids which do not occur in nucleoli[3].

The nucleus is clearly visualized in all fluorescence images (cf. e.g. figure 3.1, or also figure 3.3 and 3.4) by the DNA-specific fluorescent stain DAPI [45]. Nuclear regions with

[2] Refer to appendix D.4 for measurement statistics of all channels
[3] Refer to section 3.2.

lower content of DNA, such as nucleoli, show lower intensities due to insufficent binding of the dye, as seen in figure 3.7. Nucleoli form at specific genetic loci, the nucleolus organizer regions. They are known to rather contain rRNA and ribosomal proteins, being the location for transcription of rRNA and assembling of ribosomal subunits. LN-18 cells have been described to show large and pleomorphic nuclei [26], which is in agreement with our results. Thus, the appearance of more than one nucleolus per nucleus is not surprising. In aIF images, the nuclei can clearly be discriminated, reflected by a mean correlation coefficient $\bar{\rho} = 0.649$ (standard deviation 0.076). It is striking at the first view that the Raman pattern for the nucleus seems to give a strong enhancement on the nucleoli. Thus, it has to be assumed that constituents of the nucleus (mostly nucleic acids, more precisely, DNA) as well as constituents of the nucleoli (mainly, nucleic acids of RNA and amino acids) contribute to the barcode. This is not surprising, since three of five nucleic acids occur in both DNA and RNA, as for example alanine, for which an assignment can be found for one of the spectral lines included in the barcode of the nucleus. For those spectral lines, for which no assignments are known yet, it might be similar. Intensity changes might be due to a higher density of molecules in the nucleoli.

The endoplasmic reticulum showed to be evenly spread throughout the whole cell in fluorescence imaging, with slight enhancement in the perinuclear region and towards the periphery of the cell. This finding is consistent across different recordings, as seen in figure 3.1 and 3.4. This wide-spread formation is to be expected, since the endoplasmic reticulum builds, together with the Golgi stacks, the main substance of the cytoplasmic membraneous system. While the more centrally located rER is rather building membrane sheets, comparable to the Golgi sheets, the sER seems to arrange similar to a tubular network [82]. The aIF image channels showing the endoplasmic reticulum give a similar picture, still showing a stronger signal for the perinuclear regions, compared to the peripherical parts of the ER (see figure 3.8, column 2). The mean correlation coefficient for the ER image pairs is $\bar{\rho} = 0.593$ (standard deviation 0.273).

Imaging of the Golgi apparatus, as shown in figure 3.3 (panel 2) and figure 3.7 (panel b and d), was made possible by an antibody binding to a SNARE protein which is expressed mainly in the trans-Golgi network [9]. Fluorescent images could give the impression of the large membranous layers of the Golgi apparatus, which condense towards the perinuclear area. The Golgi apparatus is a polar system: cis-Golgi cisterns usually associate towards the ER in the central areas of the cells, while trans-Golgi stacks interact with the plasma membranes and point towards the periphery [12, 82]. Still, in higher eukaryotic cells a central localization of the Golgi system, as observed here, can be expected [12]. Figure 3.7 panel f shows the aIF channel for the Golgi apparatus. The correlation between

both imaging methods is high (cf. panel b, correlation coefficient $\rho = 0.71$), but the Golgi barcode also seems to be sensitive for certain components of the nucleoli. This might be due to the spectral proximity of lines characterizing the Golgi apparatus and the nucleus (approx. 1100 cm^{-1}).

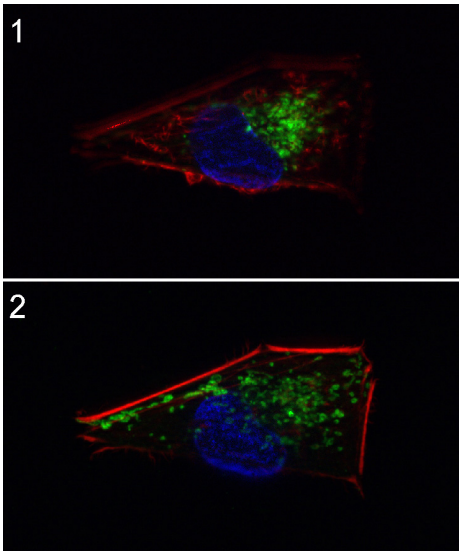

Figure 4.1: *IF: Localization of mitochondria. Notice the differences in mitochondrial distribution in the two different z-levels. (Rhodamin: Phalloidin / FITC: COX IV / DAPI)*

Mitochondria are mostly forming tubular networks, as seen in figure 3.3, panel a. Their location is varying. As shown in figure 4.1, they give a strong fluorescence signal, and their position depends on the z-focus of the fluorescence images. When observed in a focal plane close to the substrate (figure 4.1, panel 1), they assemble around the nucleus, as described "typical" for LN-18 cells [26]. At a different z-position, mitochondria again seem to form tubular structures and reach out to the cellular boundaries (cf. [7] and [82]). This is a good example for the necessity to adjust the experimental setup in a way to guarantee optimized registration. Organelle distribution varies throughout the cell, therefore both imaging techniques have to be conducted at the same focal plane. Since this cannot be achieved by manual setting, we recorded a whole z-feed of IF images with a z-offset of 0.5 µm. This later allowed to register the Raman spectral data with the best-fitting z-plane of the IF stack. Still, the z-position cannot be fully adjusted to the very same height as in Raman measurements due to the different focal depth (in z).

The mean correlation coefficient between the aIF channels for mitochondria and its respective IF images is $\bar{\rho} = 0.672$ (standard deviation 0.122). In mitochondria, as well as in the reconstructions of the endoplasmic reticulum, the perinuclear regions display higher intensities than the peripherical ones (figure 3.8 panel B3 and B5, respectively). It has to be assumed that in this region, all three organelles show higher density. LN-18 are highly proliferative cells, which means that transcription and protein biosynthesis run at a high rate. The nucleus is the center for these processes. Therefore, those organelles, which are needed for synthesis or construction of intracellular elements accumulate in its vicinity. It is not contradictory to find both the Golgi apparatus and the endoplasmic reticulum here, since their sheets are known to be stacked [12]. Mitochondria, even when building tubular systems, are small organelles, which can be situated in between those sheets to directly provide the energy needed [26, 82]

Recapitulating the aIF image quality for the five organneles, the following points should be noted: The correlation between the two image modalities for the channel displaying the cytoskeleton is low, since Raman spectroscopy seems not to be sensitive for the filamentary conformation of actin (cf. fig. 3.7, panel a and e). The correlation for the channel displaying the nucleus, on the other hand, is high and suggests a high sensitivity of the barcode for nuclear components (fig. 3.7, panel c and g).
As far as the endoplasmic reticulum is concerned, a visual evaluation of the aIF image without the knowledge of the fluorescence image is still difficult (cf. fig. 3.8, panel A2). Still, the correlation between the corresponding aIF and IF image channel is high. The Golgi complex, on the other hand, seems to be depicted very well by the aIF image (fig. 3.8, panel C4). The correlation coefficient for the image pair showing the Golgi system reflects this. Finding mitochondria (fig. 3.8, panel B3) between the Golgi membranes is not surprising, when considering mitochondrial shaping, especially in LN-18 cells [7, 26, 82]. It can be assumed, that the perinuclear region shows higher intensities in all three organelles displayed in the green channel, given by the density of those organelles in the specific localization.

An absolute quantitative interpretation of Raman intensities is not necessarily possible. Still, higher densities of a biochemical substance give rise to higher intensities of the assigned Raman spectral lines. This must also be taken into account for the substrate, on which cells are grown. Even in the non-fingerprint regions of Raman spectra, the background presents in a heterogenous way. Influence factors were seen in contribution of the object slide and temporal sequence of the experiments. Raman measurements are complex, and the measurement conditions were not fully reproducible, since during the development of the methodology they have been continuously refined. During the methodological process, different object slides have been used and measuring times were improved with respect to the requirements. Here, all factors causing inaccuracy have been eliminated statistically.
The constructed aIF images would show a better outcome if they would have been calculated directly from their respective IF image. Using a "leave-one-out“ method eliminates a risk of overfitting, but results in an aIF image of lower quality. For future experiments, standardized settings, including scanning sections, scanning times, and lateral resolution, may lead to improved precision.

Raman mapping is a vibrational spectroscopy method. Especially in medicine, it is very difficult for the investigator to read Raman spectra. It requires a lot of effort to get familiar with the underlying physical processes. Interpretation of spectra requires tedious scanning through tables and lists of assignments, which does not allow a rapid diagnosis.
The first, and very general conclusion we may draw from this work is the following: When

constructing images from Raman data, which allow straight visual interpretation, similar to classic imaging methods, it is necessary to exploit more than single line information. Instead, a complex spectral figure must be considered. First, the crucial information in Raman spectra taken from biological samples seems not to be contained only in the "fingerprint-region“ (600 - 1200 cm^{-1}) [21, 36]. Spectral lines identifying the organelles in the Raman data were particularly found in the very low (< 400 cm^{-1}) and very high (> 2800 cm^{-1}) wavenumbers. Only for the latter one, assignments are given, which mainly refer to the large shoulder in the Raman spectrum in this region as originating from CH-stretching modes in alkane chains (CH_3, CH_2, CH) [63]. This region is known to offer a high amount of information, but is not yet assigned to its biochemical origins in detail.
In contrast to a reductionistic approach, we do not rely on single spectral lines, but on sets of spectral lines describing complex features which can be assigned to the density of the respective compartment. This was accomplished in terms of a barcode approach, which filters for regions of high spectral information correlated to the organelle of interest. It should be noted again that the regions of high information content are not defined by presence of spectral peaks only. "High information content“ might also describe a lack of spectral intensity. Such, one pattern (barcode) as a whole has to be seen as a subset of wavelengths which are of particular relevance for the specific organelle.

Raman spectroscopy is a high resolution imaging technique. A number of processing steps are necessary to achieve aIF images showing different targets, since Raman data per se contains very extensive information. Thus, investigators who are not trained in the specific biophysical field can easily learn to evaluate aIF images, since these are similar to images achieved from standard bioanalytical imaging methods, such as fluorescence microscopy. With further investigation, the aIF images might eventually contain even more extractable information than nowerdays established imaging methods. This requires standardized imaging routines, to further improve both sensitivity and specificity with respect to the targeted structures.

Concluding, Raman spectroscopy proved to be a good method for nondestructive raster scanning on living glioblastoma cells. As it has been clearly shown that a construction aIF images from Raman data allows a direct visual interpretation, further applications for uses in cell biology seem desirable. Experiments revealing cellular alterations, e.g. a comparison between healthy and diseased cells on a substructural level, involving tumorous, inflammatory, or neurodegenerative processes, might be a further step towards an applicability of Raman hyperspectroscopy in medicine. Further future use might be the detection of metabolic changes in single subcellular compartments. The feasibility of Raman spec-

troscopy to capture such specific alterations, without changing the specimen itself, make the method highly interesting for investigations in molecular pathology.

5 Abstract

The present thesis evaluates the possibility of noninvasive label free imaging on living cells by means of Raman microspectroscopic mapping. For this purpose, a Raman system coupled to a green (532 nm) laser and a highly resolving CCD device, has been used. Raman hyperspectral mapping was carried out on living cells. The cells were fixed after measurements, after which further Raman mapping was carried out on the same and also on different cells. Subsequently, the cells were stained and imaged by fluorescence microscopy, revealing the position of five intracellular organelles of the very same cells, namely, the microfilamentous scaffold, the nucleus, the endoplasmic reticulum, the Golgi apparatus, and mitochondria. A one-to-one overlay of the Raman datasets and the corresponding fluorescence images resulted in a data format, in which every pixel in the Raman hyperspectral image was attributed to one of the fluorescence image. Using this overlay, for each of the five organelles, a spectral pattern could be determined. It filters out the regions of high spectral information correlated to the organelle of interest. This pattern is shown as a barcode. Spectral regions of high information content are not defined by presence of spectral peaks only, but might also describe a specific minimum spectral intensity.

When calculating these patterns, the mathematical methods were adjusted in a way to prevent overfitting by using a "leave-one-out“-technique. This way, accidental overinterpretation resulting from single pairs of images could be excluded.
In succession, from the pattern which has been worked out for every organelle imaged, artificial IF (aIF) images showing the specific organelles could be calculated from the Raman datasets. They were illustrated matching the respective color channel in the fluorescence image of the organell. The barcodes enabled the calculation of images for all five organelles, not only for the ones present in the fluorecence staining set for this specific cell. This shows that Raman images are not restricted to three color channels, but can give information on many different features of the map acquired.

The accuracy between (Raman-based) aIF images and IF images is reflected by the correlation coefficient ρ. The mean values $\bar{\rho}$ range from 0.462 (cytoskeleton) to 0.672 (mitochondria), in a total of 21 measurements considered. The highest analogy is observed in the mitochondria and the nucleus ($\bar{\rho} = 0.649$). The mean correlation coefficient for the

Golgi apparatus is $\bar{\rho} = 0.630$, for the endoplasmic reticulum it is $\bar{\rho} = 0.593$. The capability of displaying characteristics of the different organelles permits a direct interpretation of the position of the organelles, not only based on a limited number of known spectral peaks indicating certain constituents (e.g. nucleic acids, amino acids, fatty acids of sugars). The biochemical composition of an intracellular compartment is very complex. It is difficult to display it in a single Raman spectrum, since only a small number of spectral assignments is actually known. The approach using a pattern which reflects the whole multi-dimensional space of a Raman datasets, in our opinion, seems more reasonable.

The accuracy of the illustration of organelles does not fully reach the one given in fluorescence microscopy. Still, it offers essential advantages compared to other imaging methods. It is feasible on living cells and does not require extensive preparation, nor fixation or usage of markers or dyes. Cultured cells only have to be washed in PBS and are covered in PBS for examination, keeping the condition as close to cell culture as possible. The optical resolution of the pictures obtained is high, it reaches horizontally approx. 325 nm, and vertically approx. 1 µm. Measurement times are reasonably far below the live span of the cells used here. No changes have been observed which could indicate damages to the cells.

A future application of standardized imaging routines can further improve both sensitivity and specificity of this technique with respect to the targeted structures. Thus, the aIF images might eventually contain even more extractable information than nowerdays established imaging methods. The feasibility of Raman spectroscopy to capture specific alternations in living cells, without changing the specimen itself, make the method highly interesting for investigations in molecular pathology.

6 Zusammenfassung

Die vorliegende Arbeit beschreibt den Ansatz, Raman Spektroskopie als bildgebendes Verfahren zu nutzen, welches an lebenden Zellen und ohne aufwendige vorhergehende Aufbereitungen eingesetzt werden kann. Dafür wurde ein Raman-System verwendet, das mit einem grünen (532 nm) Laser und einer hochauflösenden CCD-Kamera ausgestattet ist. Raman-Spektroskopie wurde an lebenden Zellen durchgeführt, die Zellen wurden danach fixiert und weitere Messungen wurden an denselben und anderen Zellen durchgeführt. Anschließend wurden die Zellen gefärbt und mit Fluoreszenzmikroskopie auf die Lage von fünf verschiedenen Organellen hin untersucht. Dargestellt wurden das Zytoskelett, der Kern, das endoplasmatische Retikulum, der Golgiapparat und Mitochondrien. Die jeweilig korrespondierenden Raman- und Immunfluoreszenz-Bilddaten wurden eins-zu-eins übereinandergelegt, um diejenigen Punkte im Raman Datensatz zu finden, welche genau die Information enthalten, welche durch die Fluoreszenzmikroskopie dargestellt wurde. Für jedes der fünf untersuchten Organellen wurde ein „spektrales Muster“ berechnet, welches durch einen Barcode charakterisiert ist, wobei die einzelnen Streifen des Barcodes diejenigen spektralen Bereiche markieren, welche für genau dieses Organell von größtem spektralen Informationsgehalt sind. Dieser Informationsgehalt kann sowohl positiv als auch negativ sein, wobei „negativer“ Informationsgehalt z.B. bedeuten kann, dass in diesem speziellen Bereich des Spektrums ein Teil an Information, also Raman-Banden, fehlt, der sonst überall vorhanden ist. Bei der Berechnung der spezifischen Muster für jedes Organell wurden die mathematischen Methoden mit einer „leave-one-out“-Technik so angepasst, dass Überanpassung ausgeschlossen wurde, d.h. es zu keiner zufälligen Überinterpretation der Ähnlichkeiten in einem einzelnen Bildpaar kommen konnte.

Zuletzt wurden mit Hilfe der Barcodes artifizielle IF-Bilder (aIF-Bilder) aus den Raman Datensätzen berechnet, welche die einzelnen Organellen darstellen. Die Färbung der einzelnen Kanäle wurde entsprechend dem jeweiligen Fluorophor ausgewählt. Aus den Barcodes, die für jedes der fünf mit Fluoreszenzmikroskopie dargestellten Organellen erarbeitet wurden, konnten in der Folge auch die Organellen aus dem Raman-Daten als aIF-Bilder berechnet werden, welche an der jeweiligen Zelle nicht gefärbt und fluoreszenzmikroskopisch dargestellt worden waren. Dies zeigt, dass Bilder, die aus Raman-Datensätzen

errechnet werden, nicht auf drei Farbkanäle beschränkt sind, sondern in der jeweiligen Messung auf verschiedenste Informationen hin untersucht werden können.

Die Genauigkeit der aIF Bilder, im Vergleich zu den entsprechenden Fluoreszenzkanälen, wird durch den Korrelationskoeffizienten ρ wiedergegeben. Je nach dargestelltem Organell liegt der Mittelwert $\bar{\rho}$ zwischen 0.462 (Zytoskelett) und 0.672 (Mitochondrien), wobei insgesamt 21 Messungen berücksichtigt wurden. Die beste Übereinstimmung findet sich bei den Mitochondrien und dem Nukleus ($\bar{\rho} = 0.649$). Für das endoplasmatische Retikulum ist $\bar{\rho} = 0.593$, für den Golgi-Apparat $\bar{\rho} = 0.630$. Durch die Möglichkeit, spezifische Charakteristika der Organellen herauszufiltern, erlaubt das rekonstruierte Bild ein direktes Urteil über die Lage der Organellen, nicht nur über gewisse biochemische Zusammensetzungen (wie z.B. Nukleinsäuren, Aminsäuren, Fette oder Zucker), wie es bisher von Raman-Bildern bekannt war.

Die Darstellung der Organellen erreicht die Genauigkeit von Immunfluoreszenzfärbungen nicht gänzlich. Sie bietet jedoch wesentliche Vorteile gegenüber anderen bildgebenden Verfahren: Sie ist an lebenden Zellen anwendbar und verlangt keine aufwendigen vorhergehenden Bearbeitungen oder Veränderungen der Proben. Fixierung sowie Anwendung von exogenen Stoffen, beispielsweise Antikörpern oder Farbstoffen, ist nicht nötig. Die Kulturzellen müssen nur in PBS gewaschen werden, die Messung findet in PBS-Immersion statt und ist damit so nahe an den Zellkulturbedingungen wie möglich. Die optische Auflösung, welche so in den Bildern erreicht werden kann, ist hoch. Sie erreicht horizontal ca. 325 nm und vertikal ca. 1 µm. In unserem Fall liegen die Messzeiten um mehr als eine Größenordnung niedriger als die Lebensspanne der Zellen, und es wurden keinerlei Veränderungen beobachtet, die auf eine verminderte Lebensfähigkeit der Zelle schließen lassen könnten.

Zukünftige Anwendung eines vollständig standardisierten experimentellen Ablaufs können sowohl die Sensitivität als auch die Spezifität dieses Verfahrens im Bezug auf die darzustellenden Strukturen verbessern. So könnte ein aIF-Bild sogar mehr nutzbare Information als heutzutage etablierte bildgebende Methoden in der Zellbiologie bringen. Raman-Spektroskopie bietet eine Möglichkeit, spezifische, feinste Veränderungen in lebenden Zellen erfassen zu können, ohne diese selbst zu verändern. Damit ist sie von höchstem Interesse für Felder wie die molekulare Pathologie.

Bibliography

[1] B. Alberts, A. Johnson, J. Lewis, M. Raff, K. Roberts, and P. Walter. Molecular Biology of the Cell. Garland Science, New York, 4. edition, march 2002.

[2] N. Amharref, A. Beljebbar, S. Dukic, L. Venteo, L. Schneider, M. Pluot, and M. Manfait. Discriminating healthy from tumor and necrosis tissue in rat brain tissue samples by Raman spectral imaging. Biochim Biophys Acta, 1768(10):2605–15, 2007.

[3] M. Baker. Laser tricks without labels. Nature Methods, 7:261–266, 2010.

[4] H. N. Banerjee and L. Zhang. Deciphering the finger prints of brain cancer astrocytoma in comparison to astrocytes by using near infrared Raman spectroscopy. Mol Cell Biochem, 295(1-2):237–40, 2007.

[5] J. A. Barden, M. Miki, B. D. Hambly, and C. G. dos Remedios. Localization of the phalloidin and nucleotide-binding sites on actin. European Journal of Biochemistry, 162(3):583–588, 1987.

[6] A. Barrientos, M. H. Barros, I. Valnot, A. Rötig, P. Rustin, and A. Tzagoloff. Cytochrome oxidase in health and disease. Gene, 286(1):53 – 63, 2002. Papers presented at the International Meeting "Mitochondria:Evolution, Genomics, Homeostasis and Pathology", Selva di Fasano (BR, Italy), 9-12 May 2001.

[7] J. Bereiter-Hahn. Behavior of Mitochondria in the Living Cell. volume 122 of International Review of Cytology, pages 1 – 63. Academic Press, 1990.

[8] M. S. Bergholt, W. Zheng, K. Lin, K. Y. Ho, M. Teh, K. G. Yeoh, J. B. Yan So, and Z. Huang. Raman endoscopy for in vivo differentiation between benign and malignant ulcers in the stomach. Analyst, 135:3162–3168, 2010.

[9] J. B. Bock, J. Klumperman, S. Davanger, and R. H. Scheller. Syntaxin 6 functions in trans-Golgi network vesicle trafficking. Molecular Biology of the Cell, 8(7):1261–71, 1997.

[10] J. B. Bock, L. C. Lin, and R. H. Scheller. A New Syntaxin Family Member Implicated in Targeting of Intracellular Transport Vesicles. Journal of Biological Chemistry, 271(30):17961–17965, 1996.

[11] J. B. Bock, H. T. Matern, A. A. Peden, and R. H. Scheller. A genomic perspective on membrane compartment organization. Nature, 409(2001/02/14/print):839 – 841, 2001.

[12] M. Bornens. Organelle positioning and cell polarity. Nat. Rev. Mol. Cell. Biol., 9:874 – 886, 11 2001.

[13] C. M. Brown. Fluorescence microscopy - avoiding the pitfalls. Journal of Cell Science, 120(10):1703–1705, 2007.

[14] P. R. Carey. Raman crystallography and other biochemical applications of Raman microscopy. Annu Rev Phys Chem, 57:527–54, 2006.

[15] P. J. Caspers, G. W. Lucassen, E. A. Carter, H. A. Bruining, and G. J. Puppels. In Vivo Confocal Raman Microspectroscopy of the Skin: Noninvasive Determination of Molecular Concentration Profiles. Journal of Investigative Dermatology, 116(3):434–442, 2001.

[16] J. W. Chan and D. K. Lieu. Label-free biochemical characterization of stem cells using vibrational spectroscopy. Journal of Biophotonics, 2(11):656–668, 2009.

[17] J. Cheng and X. S. Xie. Coherent Anti-Stokes Raman Scattering Microscopy: Instrumentation, Theory, and Applications. The Journal of Physical Chemistry B, 108(3):827–840, 2004.

[18] L.-P. Choo-Smith, H. G. M. Edwards, H. P. Endtz, J. M. Kros, F. Heule, H. Barr, J. S. Robinson, H. A. Bruining, and G. J. Puppels. Medical applications of Raman spectroscopy: From proof of principle to clinical implementation. Biopolymers, 67(1):1–9, 2002.

[19] P. Colomban. Raman analyses and "smart" imaging of nanophases and nanosized materials. Spectroscopy Europe, 15, 2003.

[20] J. A. Cooper. Effects of Cytochalasin and Phalloidin on Actin. The Journal of Cell Biology, 105:1473 – 1478, 10 1987.

[21] J. De Gelder, K. De Gussem, P. Vandenabeele, and L. Moens. Reference database of Raman spectra of biological molecules. Journal of Raman Spectroscopy, 38(9):1133–1147, 2007.

[22] J. De Gelder, K. De Gussem, P. Vandenabeele, M. Vancanneyt, P. De Vos, and L. Moens. Methods for extracting biochemical information from bacterial Raman spectra: focus on a group of structurally similar biomolecules–fatty acids. Anal Chim Acta, 603(2):167–75, 2007.

[23] K. De Gussem, P. Vandenabeele, A. Verbeken, and L. Moens. Chemotaxonomical identification of spores of macrofungi: possibilities of raman spectroscopy. Analytical and Bioanalytical Chemistry, 387:2823–2832, 2007. 10.1007/s00216-007-1150-1.

[24] M. A. De Matteis and A. Luini. Exiting the Golgi complex. Nat. Rev. Mol. Cell. Biol., 9:273 – 284, 04 2008.

[25] M. Diem, M. Romeo, S. Boydston-White, M. Miljkovic, and C. Matthaus. A decade of vibrational micro-spectroscopy of human cells and tissue (1994-2004). Analyst, 129(10):880–5, 2004.

[26] A. C. Diserens, N. de Tribolet, A. Martin-Achard, A. C. Gaide, J. F. Schnegg, and S. Carrel. Characterization of an established human malignant glioma cell line: LN-18. Acta Neuropathol, 53(1):21–8, 1981.

[27] S. Dochow, C. Krafft, U. Neugebauer, T. Bocklitz, T. Henkel, G. Mayer, J. Albert, and J. Popp. Tumour cell identification by means of Raman spectroscopy in combination with optical traps and microfluidic . Lab Chip, 11:1484–1490, 2011.

[28] G. J. Doherty and H. T. McMahon. Mediation, Modulation, and Consequences of Membrane-Cytoskeleton Interactions. Annual Review of Biophysics, 37(1):65–95, 2008. PMID: 18573073.

[29] F. Draux, C. Gobinet, J. Sulé-Suso, A. Trussardi, M. Manfait, P. Jeannesson, and G. Sockalingum. Raman spectral imaging of single cancer cells: probing the impact of sample fixation methods. Analytical and Bioanalytical Chemistry, 397:2727–2737, 2010. 10.1007/s00216-010-3759-8.

[30] H. G. M. Edwards. Probing history with raman spectroscopy. Analyst, 129:870–879, 2004.

[31] Nobel Foundation. Noble Lectures, Physics 1922-1941. Elsevier Publishing Company, Amsterdam, 1965.

[32] C. W. Freudiger, W. Min, B. G. Saar, S. Lu, G. R. Holtom, C. He, J. C. Tsai, J. X. Kang, and X. S. Xie. Label-Free Biomedical Imaging with High Sensitivity by Stimulated Raman Scattering Microscopy. Science, 322(5909):1857–1861, 2008.

[33] A. Frey-Wyssling. Concerning the concept 'organelle'. Cellular and Molecular Life Sciences, 34:547–547, 1978. 10.1007/BF01935984.

[34] H. Fukunaga, H. Yoshimura, Y. Nishina, Y. Nagashima, and M. Tachibana. Label-free biomedical imaging of hydrodynamics in single human cells. Biomedical Research, 31(3):177–181, 2010.

[35] G. Gouadec and P. Colomban. Raman Spectroscopy of nanomaterials: How spectra relate to disorder, particle size and mechanical properties. Progress in Crystal Growth and Characterization of Materials, 53(1):1 – 56, 2007.

[36] J. Griffiths. Raman spectroscopy for medical diagnosis. Anal Chem, 79(11):3975–8, 2007.

[37] A. S. Haka, K. E. Shafer-Peltier, M. Fitzmaurice, J. Crowe, R. R. Dasari, and M. S. Feld. Diagnosing breast cancer by using Raman spectroscopy. Proceedings of the National Academy of Sciences of the United States of America, 102(35):12371–12376, 2005.

[38] K. Hamada, K. Fujita, N. I. Smith, M. Kobayashi, Y. Inouye, and S Kawata. Raman microscopy for dynamic molecular imaging of living cells. J. Biomed. Opt., 13(4):044027–1 – 044027–4, 2008.

[39] E. B. Hanlon, R. Manoharan, T.-W. Koo, K. E. Shafer, J.T. Motz, M. Fitzmaurice, J. R. Kramer, I. Itzkan, R. R. Dasari, and M.S. Feld. Prospects for in vivo Raman spectroscopy. Physics in Medicine and Biology, 45(2):R1, 2000.

[40] R. C. Hawes, K. P. George, D. C. Nelson, and R. Beckwith. Laser excitation of Raman spectra. Analytical Chemistry, 38(13):1842–1847, 1966.

[41] S. Hoey, D. H. Brown, A. A. McConnell, W. E. Smith, M. Marabani, and R. D. Sturrock. Resonance Raman spectroscopy of hemoglobin in intact cells: A probe of oxygen uptake by erythrocytes in rheumatoid arthritis. Journal of Inorganic Biochemistry, 34(3):189 – 199, 1988.

[42] J. Horsnell, P. Stonelake, J. Christie-Brown, G. Shetty, J. Hutchings, C. Kendall, and N. Stone. Raman spectroscopy-A new method for the intra-operative assessment of axillary lymph nodes. Analyst, 135:3042–3047, 2010.

[43] P. R. Jess, D. D. Smith, M. Mazilu, K. Dholakia, A. C. Riches, and C. S. Herrington. Early detection of cervical neoplasia by Raman spectroscopy. Int J Cancer, 121(12):2723–8, 2007.

[44] L. V. Johnson, M. L. Walsh, and L. B. Chen. Localization of mitochondria in living cells with rhodamine 123. Proceedings of the National Academy of Sciences, 77(2):990–994, 1980.

[45] J. Kapuscinski. DAPI: a DNA-Specific Fluorescent Probe. Biotech. Histochem., 70(5):220–233, 1995.

[46] M. Kazanci, P. Roschger, E. P. Paschalis, K. Klaushofer, and P. Fratzl. Bone osteonal tissues by Raman spectral mapping: Orientation-composition. Journal of Structural Biology, 156(3):489 – 496, 2006.

[47] S. Keren, C. Zavaleta, Z. Cheng, A. de la Zerda, O. Gheysens, and S. S. Gambhir. Noninvasive molecular imaging of small living subjects using Raman spectroscopy. Proceedings of the National Academy of Sciences, 105(15):5844–5849, 2008.

[48] C. Kirschner, K. Maquelin, P. Pina, N. A. Ngo Thi, L.-P. Choo-Smith, G. D. Sockalingum, C. Sandt, D. Ami, F. Orsini, S. M. Doglia, P. Allouch, M. Mainfait, G. J. Puppels, and D. Naumann. Classification and Identification of Enterococci: a Comparative Phenotypic, Genotypic, and Vibrational Spectroscopic Study. J. Clin. Microbiol., 39(5):1763–1770, 2001.

[49] K. Klein, A. Gigler, T. Aschenbrenner, R. Monetti, W. Bunk, F. Jamitzky, G. Morfill, R. Stark, and J. Schlegel. Label-free live cell imaging with confocal raman microscopy. Biophysical Journal, 2011, accepted for publication.

[50] H. Kornfeld. Bemerkung zu der Mitteilung von G. Landsberg und L. Mandelstam über eine neue Erscheinung in der Lichtzerstreuung in Krystallen. Naturwissenschaften, 16:653–653, 1928.

[51] C. Krafft. Bioanalytical applications of Raman spectroscopy. Analytical and Bioanalytical Chemistry, 378:60–62, 2004.

[52] C. Krafft, T. Knetschke, R. H. Funk, and R. Salzer. Studies on stress-induced changes at the subcellular level by Raman microspectroscopic mapping. Anal Chem, 78(13):4424–9, 2006.

[53] C. Krafft, L. Neudert, T. Simat, and R. Salzer. Near infrared Raman spectra of human brain lipids. Spectrochim Acta A Mol Biomol Spectrosc, 61(7):1529–35, 2005.

[54] C. Krafft, S. B. Sobottka, G. Schackert, and R. Salzer. Near infrared Raman spectroscopic mapping of native brain tissue and intracranial tumors. Analyst, 130(7):1070–7, 2005.

[55] C. Krafft, S. B. Sobottka, G. Schackert, and R. Salzer. Raman and infrared spectroscopic mapping of human primary intracranial tumors: a comparative study. Journal of Raman Spectroscopy, 37(1-3):367–375, 2006.

[56] C. Krafft, K. Thümmler, S. B. Sobottka, G. Schackert, and R. Salzer. Classification of malignant gliomas by infrared spectroscopy and linear discriminant analysis. Biopolymers, 82(4):301–305, 2006.

[57] J. W. Lichtman and J.-A. Conchello. Fluorescence microscopy. Nature Methods, 2:910–919, 2005.

[58] D. A. Long. The Raman Effect. A Unified Treatment of the Theory of Raman Scattering by Molecules. John Wiley & Sons Ltd, West Sussex PO19 1UD, England, 2002.

[59] K. Maquelin, L.-P. Choo-Smith, H. P. Endtz, H. A. Bruining, and G. J. Puppels. Rapid identification of candida species by confocal raman microspectroscopy. J. Clin. Microbiol., 40(2):594–600, 2002.

[60] K. Maquelin, L.-P. Choo-Smith, C. Kirschner, N.A. Ngo-Thi, D. Naumann, and G.J. Puppels. Vibrational Spectroscopic Studies of Microorganisms. John Wiley & Sons, Ltd, 2006.

[61] K. Maquelin, C. Kirschner, L.-P. Choo-Smith, N. van den Braak, H. Ph. Endtz, D. Naumann, and G. J. Puppels. Identification of medically relevant microorganisms by vibrational spectroscopy. Journal of Microbiological Methods, 51(3):255 – 271, 2002.

[62] C. Matthaus, S. Boydston-White, M. Miljkovic, M. Romeo, and M. Diem. Raman and infrared microspectral imaging of mitotic cells. Appl Spectrosc, 60(1):1–8, 2006.

[63] C. Matthaus, T. Chernenko, J. A. Newmark, C. M. Warner, and M. Diem. Label-free detection of mitochondrial distribution in cells by nonresonant Raman microspectroscopy. Biophys J, 93(2):668–73, 2007.

[64] C. Matthaus, A. Kale, T. Chernenko, V. Torchilin, and M. Diem. New ways of imaging uptake and intracellular fate of liposomal drug carrier systems inside individual cells, based on Raman microscopy. Mol Pharm, 5(2):287–93, 2008.

[65] A. Meade, C. Clarke, F. Draux, G. Sockalingum, M. Manfait, F. Lyng, and H. Byrne. Studies of chemical fixation effects in human cell lines using Raman microspectroscopy. Analytical and Bioanalytical Chemistry, 396:1781–1791, 2010. 10.1007/s00216-009-3411-7.

[66] S Mogelsvang, B. J. Marsh, M. S. Ladinsky, and K. E. Howell. Predicting Function from Structure: 3D Structure Studies of the Mammalian Golgi Complex. Traffic, 5(5):338–345, 2004.

[67] New England Biolabs GmbH, Brüningstr. 50, Geb. B852, 65926 Frankfurt am Main, Germany. Syntaxin 6 (C34B2) Rabbit mAb, 2010. Cell Signaling Technology No. 2869.

[68] New England Biolabs GmbH, Brüningstr. 50, Geb. B852, 65926 Frankfurt am Main, Germany. Calnexin Antibody, 2011. Cell Signaling Technology No. 2433.

[69] New England Biolabs GmbH, Brüningstr. 50, Geb. B852, 65926 Frankfurt am Main, Germany. COX IV (3E11) Rabbit mAb, 2011. Cell Signaling Technology No. 4850.

[70] I. Notingher, I. Bisson, A. E. Bishop, W. L. Randle, J. M. Polak, and L. L. Hench. In situ spectral monitoring of mRNA translation in embryonic stem cells during differentiation in vitro. Anal Chem, 76(11):3185–93, 2004.

[71] I. Notingher and L. L. Hench. Raman microspectroscopy: a noninvasive tool for studies of individual living cells in vitro. Expert Rev Med Devices, 3(2):215–34, 2006.

[72] I. Notingher, S. Verrier, S. Haque, J. M. Polak, and L. L. Hench. Spectroscopic study of human lung epithelial cells (A549) in culture: living cells versus dead cells. Biopolymers, 72(4):230–40, 2003.

[73] C. A. Owen, I. Notingher, R. Hill, M. Stevens, and L. L. Hench. Progress in Raman spectroscopy in the fields of tissue engineering, diagnostics and toxicological testing. J Mater Sci Mater Med, 17(11):1019–23, 2006.

[74] F. C. Pascut, H. T. Goh, V. George, C. Denning, and I. Notingher. Toward label-free Raman-activated cell sorting of cardiomyocytes derived from human embryonic stem cells. Journal of Biomedical Optics, 16(4):045002, 2011.

[75] J. Pawley, editor. Handbook of biological confocal microscopy. Springer Verlag, New York, 3. edition, 2006.

[76] Plano Elektronenmikroskopie, Wetzlar, Germany. Zubehör für Lichtmikroskopie.

[77] V. V. Pully and C. Otto. The intensity of the 1602 cm^{-1} band in human cells is related to mitochondrial activity. Journal of Raman Spectroscopy, 40(5):473–475, 2009.

[78] G. J. Puppels, F. F. de Mul, C. Otto, J. Greve, M. Robert-Nicoud, D. J. Arndt-Jovin, and T. M. Jovin. Studying single living cells and chromosomes by confocal Raman microspectroscopy. Nature, 347(6290):301–3, 1990.

[79] G. J. Puppels, H. S. Garritsen, G. M. Segers-Nolten, F. F. de Mul, and J. Greve. Raman microspectroscopic approach to the study of human granulocytes. Biophys J, 60(5):1046–56, 1991.

[80] G. J. Puppels, J. H. F. Olminkhof, G. M. J. Segers-Nolten, C. Otto, F. F. M. F. F. M. de Mul, and J. Greve. Laser irradiation and Raman spectroscopy of single living cells and chromosomes: Sample degradation occurs with 514.5 nm but not with 660 nm laser light. Experimental Cell Research, 195(2):361 – 367, 1991.

[81] G. Pyrgiotakis, O. Kundakcioglu, K. Finton, P. Pardalos, K. Powers, and B. Moudgil. Cell Death Discrimination with Raman Spectroscopy and Support Vector Machines. Annals of Biomedical Engineering, 37:1464–1473, 2009. 10.1007/s10439-009-9688-z.

[82] S. M. Rafelski and W. F. Marshall. Building the cell: design principles of cellular architecture. Nat. Rev. Mol. Cell. Biol., 9(5):593–602, 08 2008.

[83] S. Rajagopalan, Y. Xu, and M. B. Brenner. Retention of unassembled components of integral membrane proteins by calnexin. Science, 263(5145):387–390, 1994.

[84] C. V. Raman and K. S. Krishnan. The Optical Analogue of the Compton Effect. Nature, 121, 1928.

[85] M. Scholtes-Timmerman, H. Willemse-Erix, T. B. Schut, A. van Belkum, G. Puppels, and K. Maquelin. A novel approach to correct variations in Raman spectra due to photo-bleachable cellular components. Analyst, 134:387–393, 2009.

[86] O. Shimomura, F. H. Johnson, and Y. Saiga. Extraction, Purification and Properties of Aequorin, a Bioluminescent Protein from the Luminous Hydromedusan, Aequorea. Journal of Cellular and Comparative Physiology, 59(3):223–239, 1962.

[87] D. C. Smith. A review of the non-destructive identification of diverse geomaterials in the cultural heritage using different configurations of Raman spectroscopy. Geological Society, London, Special Publications, 257(1):9–32, 2006.

[88] K. R. Spring and M. W. Davidson. Introduction to Fluorescence Microscopy. `http://www.microscopyu.com/print/articles/fluorescence/fluorescenceintro-print.html`. Stand: 03. 08. 2011.

[89] P. C. Stair. Advances in Raman spectroscopy methods for catalysis research. Current Opinion in Solid State and Materials Science, 5(5):365 – 369, 2001.

[90] M. A. Strehle, P. Rosch, R. Petry, A. Hauck, R. Thull, W. Kiefer, and J. Popp. A Raman spectroscopic study of the adsorption of fibronectin and fibrinogen on titanium dioxide nanoparticles. Physical Chemistry Chemical Physics, 6(22):5232–5236, 2004.

[91] T. C. Strekas and T. G. Spiro. Cytochrome c: Resonance Raman spectra. Biochimica et Biophysica Acta (BBA) - Protein Structure, 278(1):188 – 192, 1972.

[92] T. G. Strekas and T. G. Spiro. Hemoglobin: Resonance Raman spectra. Biochimica et Biophysica Acta (BBA) - Protein Structure, 263(3):830 – 833, 1972.

[93] R. J. Swain, G. Jell, and M. M. Stevens. Non-invasive analysis of cell cycle dynamics in single living cells with Raman micro-spectroscopy. J Cell Biochem, 104(4):1427–38, 2008.

[94] R. J. Swain and M. M. Stevens. Raman microspectroscopy for non-invasive biochemical analysis of single cells. Biochem Soc Trans, 35(Pt 3):544–9, 2007.

[95] G. J. Thomas Jr. Raman Spectroscopy of Protein and Nucleic Acid Assemblies. Annual Review of Biophysics and Biomolecular Structure, 28:1–27, 1999.

[96] T. Tsukihara, H. Aoyama, E. Yamashita, T. Tomizaki, H. Yamaguchi, K. Shinzawa-Itoh, R. Nakashima, R. Yaono, and S. Yoshikawa. The Whole Structure of the 13-Subunit Oxidized Cytochrome c Oxidase at 2.8 Å. Science, 272(5265):1136–1144, 1996.

[97] N. Uzunbajakava, A. Lenferink, Y. Kraan, E. Volokhina, G. Vrensen, J. Greve, and C. Otto. Nonresonant confocal Raman imaging of DNA and protein distribution in apoptotic cells. Biophys J, 84(6):3968–81, 2003.

[98] N. Uzunbajakava, A. Lenferink, Y. Kraan, B. Willekens, G. Vrensen, J. Greve, and C. Otto. Nonresonant Raman imaging of protein distribution in single human cells. Biopolymers, 72(1):1–9, 2003.

[99] N. Uzunbajakava and C. Otto. Combined Raman and continuous-wave-excited two-photon fluorescence cell imaging. Opt. Lett., 28(21):2073–2075, Nov 2003.

[100] H. J. van Manen, Y. M. Kraan, D. Roos, and C. Otto. Single-cell Raman and fluorescence microscopy reveal the association of lipid bodies with phagosomes in leukocytes. Proc Natl Acad Sci U S A, 102(29):10159–64, 2005.

[101] P. Vandenabeele, H. G. M. Edwards, and L. Moens. A Decade of Raman Spectroscopy in Art and Archaeology. Chemical Reviews, 107(3):675–686, 2007.

[102] S. Verrier, I. Notingher, J. M. Polak, and L. L. Hench. In situ monitoring of cell death using Raman microspectroscopy. Biopolymers, 74(1-2):157–62, 2004.

[103] W. H. Weber and R. Merlin. Raman Scattering in Material Science. Springer Verlag, Berlin, Heidelberg, 2000.

[104] T. Wieland. Interaction of phallotoxins with actin. Advances in Enzyme Regulation, 15:285 – 299, 1977.

[105] D. B. Williams. Beyond lectins: the calnexin/calreticulin chaperone system of the endoplasmic reticulum. Journal of Cell Science, 119(4):615–623, 2006.

[106] WITec. alpha300R Confocal Raman Microscope. Lise-Meitner-Straße 6, D-89081 Ulm, Germany. www.WITec.de.

[107] F. S. Wouters. The physics and biology of fluorescence microscopy in the life sciences. Contemporary Physics, 47(5):239–255, 2006.

[108] H. Wu, J. V. Volponi, A. E. Oliver, A. N. Parikh, B. A. Simmons, and S. Singh. In vivo lipidomics using single-cell Raman spectroscopy. Proceedings of the National Academy of Sciences, 108(9):3809–3814, 2011.

[109] E. Wulf, A. Deboben, F. A. Bautz, H. Faulstich, and T. Wieland. Fluorescent phallotoxin, a tool for the visualization of cellular actin. Proceedings of the National Academy of Sciences, 76(9):4498–4502, 1979.

[110] Y. Yeni, J. Yerramshetty, O. Akkus, C. Pechey, and C. Les. Effect of Fixation and Embedding on Raman Spectroscopic Analysis of Bone Tissue. Calcified Tissue International, 78:363–371, 2006. 10.1007/s00223-005-0301-7.

[111] A. B. Zoladek, R. K. Johal, S. Garcia-Nieto, F. Pascut, K. M. Shakesheff, A. M. Ghaemmaghami, and I. Notingher. Label-free molecular imaging of immunological synapses between dendritic and T cells by Raman micro-spectroscopy. Analyst, 135:3205–3212, 2010.

[112] E. Zuser, T. Chernenko, J. Newmark, M. Miljkovic, and M. Diem. Confocal Raman microspectral imaging (CRMI) of murine stem cell colonies. Analyst, 135:3030–3033, 2010.

Appendix

A Assignments

peak (cm^{-1})	Assignment			
	DNA/RNA	*Proteins*	*Lipids*	*Carbohydrates*
621		C-C twist Phe		
645		C-C twist Tyr		
667	Th, Gu			
671		C-S stretching Cys		
681	Gu ring breathing			
717			$CN^+(CH_3)_3$ stretching	
719			C-C-N^+ symm. stretching in phosphatidylcholine (membranes)	
720	C-N stretching A		C-N stretching	
729	Ad			
755-760		Symmetric ring breathing in Trp		
782-785	Ur, Cy, Th ring breathing			
788	O-P-O backbone stretching/Th/Cy			
800-1100			C-O-C vibrations of glycosidic bonds and sugar rings	
811	RNA: C_5-O-P-O-C_3 phosphodiester bonds stretching			
828-833	DNA: O-P-O backbone stretching	out of plane ring breathing in Tyr		
854		Ring breathing in Tyr/C-C stretching in Pro		
877			C-C-N^+ symmetric stretching	Carbohydrate: C-O-H ring
900		C-C skeletal stretching		
937-939		C-C skeletal stretching (α-helix)		C-O-H glycosylation
980	C-C BK stretch β-sheet		=CH bend in lipids	
1005		Symmetric ring breathing mode of Phe		
1033-1036		C-H in plane bending mode of Phe		
1060-1095	DNA: O-P-O backbone stretching		chain C-C stretch	C-O, C-C stretching
1095			PO_2^-: symmetric stretching mode of phosphate esters	
1128		C-N stretch		C-O stretch in carbohydrates
1129			skeletal C-C stretching	
1158		C-C/C-N stretching		
1176		C-H bend Tyr		
1180	Cy, Gu, Ad			
1209		C-C_6H_5 stretch in Phe, Try		
1220-1284	DNA: Th, Ad	Amide III: β-sheed	=CH bend	
1250-1350		Extended amide III: coupled C-H, N-H deformation modes, peptide backbone		

1258	Ad, Cy	Amide III: β-sheed	
1301-1308	CH_2 deformation in Ad, Cy		CH_2 deformation
1320	Gu	CH def.	
1340-1342	Polynucleotide chain; DNA: Ad, Gu		
1420-1480	Ad, Gu		
1425-1475		peptide side chains	CH_2 and CH_3 deformations: antisymmetric methyl and methylene deformation, phospholipids
1449		C-H vibrations	C-H vibrations (aminoacids, lipids)
1452			CH_2 deformation
1460		Fibronectin (?)	methyl and methylene deformations
1476		Fibronectin (?)	
1553		C-C stretching (Trp)	
1575-1582	Gu, Ad (C=C ring stretching modes)		
1602		Mitochondria (molecular species=?)	
1607-1610		C=C binding in Phe, Tyr	
1617		C=C binding in Try, Tyr	
1650-1680		Amide I: α-helix, C=C-stretch	
1655		Amide I: C=O stretching mode, peptide linkage	
1660			C-C stretching
1670	T (C=O)		
1736			C-O ester in lipids
2800-3020		CH-stretching modes (CH3, CH2, CH)	

Assignment of Raman peaks found in biological specimen[22, 43, 62, 63, 71, 79, 90]

B Materials, facilities

B.1 Cell culture

MATERIAL	PROVIDER
LN-18	Division of Neuropathology, Institute of Pathology, Technische Universität München, Ismaninger Str. 22, 81675 Munich, Germany
England Finder	Plano Elektronenmikroskopie, Ernst-Befort-Strasse 12, 35578 Wetzlar, Germany
Quadriperm culture flasks	Greiner Bio-One GmbH, Maybachstrasse 2, 72636 Frickenhausen, Germany
DMEM	GIBCO Invitrogen Cell Culture, 3 Fountain Drive, Inchinnan Business Park, Paisley PA4 9RF, UK
fetal calf serum penicillin streptomycin glutamine	Biochrom AG, Leonorenstr. 2-6, 12247 Berlin Germany
PBS	PAA Laboratories, Haidmannweg 9, 4061 Pasching, Austria

B.2 Raman microspectroscopy equipment

DEVICE	MANUFACTURER
Raman microscope alpha 300R	WITec Wissenschaftliche Instrumente und Technologie GmbH, Lise-Meitner-Str. 6, 89081 Ulm, Germany

MATERIAL	PROVIDER
aluminium Petri dish	Laboratories of the Department of Earth and Environmental Sciences, Ludwig-Maximilians-Universität München, Theresienstr. 41, 80333 Munich, Germany
PBS	PAA Laboratories, Haidmannweg 9, 4061 Pasching, Austria
phosphate buffered formalin solution	Carl Roth GmbH & Co KG, Schoemperlenstraße 1-5, 76185 Karlsruhe, Germany

B.3 Immunofluorescence staining

SUBSTANCE	PROVIDER
Calnexin antibody, COX IV (3E11) Rabbit mAb, Syntaxin 6 (C34B2) Rabbit mAb	New England Biolabs, Brüningstr. 50, 65929 Frankfurt am Main, Germany
FITC	Zymed Laboratories, 458 Carlton Court S., San Francisco, CA 94080, USA
rhodamin-conjugated phalloidin, DAPI	Sigma-Aldrich Chemie GmbH, Eschenstrasse 5, 82024 Taufkirchen, Germany
Vectashield mounting medium	Linaris Biologische Produkte GmbH, Frankenweg 18, 69221 Dassenheim, Germany

B.4 Fluorescence microscopy equipment

DEVICE	MANUFACTURER
AxioImager, AxioVision 4.5	Carl Zeiss Jena GmbH, Carl-Zeiss-Promenade 10, 07745 Jena, Germany

B.5 Institutes involved

Division of Neuropathology
Institute of Pathology
Technische Universität München
Trogerstr. 18
81675 Munich
Germany

Department of Earth and Environmental Sciences
Ludwig-Maximilians-Universität München
Theresienstr. 41
80333 Munich
Germany

Max-Planck-Institute for Extraterrestrial Physics
Giessenbachstrasse
85741 Garching
Germany

C Protocols

C.1 Cell handling

CULTURE CONDITIONS	
numerating of England Finders to avoid mistaken identity culture placement: England Finder in Quadriperm culture flasks	
incubation (37° C, 5% CO_2) in DMEM + 10% fetal calf serum + 100 U/ml penicillin + 100 µg/ml streptomycin, + 2 mMol/ml glutamine[1]	48 - 72h
transport from incubator in the laboratories of the Division of Neuropathology to the Department of Earth and Environmental Sciences[2] in an insulating styrofoam box on warm-packs (37° C)	max. 30’
storage in the incubator of the Department of Earth and Environmental Sciences at 37° C, environment atmosphere	$\frac{1}{2}$ – 8h
BEFORE RAMAN MAPPING:	
washing in PBS (37° C)	3 × 1’
positioning in aluminium Petri dish; fixation with clamps,	
covering in PBS (37° C)	$\frac{1}{2}$ – max. 4h
BETWEEN MEASUREMENTS	
rinsing in PBS (37° C)	3 × 1’
AFTER RAMAN MAPPING:	
careful unscrewing and removing the slide from the petri dish	
washing in PBS (37° C)	3 × 1’
fixation in 4% phosphate buffered formalin solution	20’
washing in PBS (37° C)	3 × 1’
storage covered in PBS at 4° C until further use	

[1] for references, see section B
[2] for addresses, see section B.5

C.2 Raman mapping

microscope fine calibration	10.0 mW

positioning of the aluminium Petri dish on the scan table, alignment of England Finder grating orthagonal to the microscopical field by microscopical inspection and manual adjustment;
selection of 1-4 viable, spread-out cells under light-microscopical control;

exact notes on position and shape of the cells, technical details, and, where necessary, specific conditions in the laboratory logbook

RAMAN SPECTRAL MAPPING[3]:

spectral integration time	0.07 s/pixel
working panel	50×70 µm
spatial resolution	100×140 – 150×210 pixel

in ca. 50% of all cases repetition of measurements after formalin fixation on the very same cells and with the same setup

C.3 Immunofluorescence staining

C.3.1 Dilutions

FITC	1:100[4]
Phalloidin	1:800[5]
Calnexin antibody	1:100[6]
COX IV (3E11) Rabbit mAb	1:100[7]
Syntaxin 6 (C34B2) Rabbit mAb	1:100[8]

[3] exemplary: typical raster-scanning setup
[4] protocols established in the laboratories of the Division of Neuropathology
[5] protocols established in the laboratories of the Division of Neuropathology
[6] after establishment with different concentrations (1:50, 1:100, 1:200, 1:250)
[7] after establishment with different concentrations (1:50, 1:100, 1:200, 1:250)
[8] after establishment with different concentrations (1:50, 1:100, 1:200, 1:250)

Exemplary volumes calulated for one slide:

primary antibody dilution:	
antibody	4 µl
+ antibody diluent solution	396 µl
secondary antibody dilution:	
antibody diluent solution	395.5 µl
+ goat anti rabbit FITC	4 µl
+ Phalloidin	0.5 µl
DAPI dilution:	
PBS	100 ml
+ Hoechst-dye	20 µl

C.3.2 Staining protocol

0.25% Triton x-low/PBS	10’
wash in PBS	3 × 1’
50 mMol NH_4Cl	10’
wash in PBS	3 × 1’
clean edges (ca. 2 mm each side) horizontal positioning in humid compartment	
incubation with 300 µl goat serum	30’
withdraw goat serum from slides by capillary suction (absorbent tissue paper) clean edges	
pipette 400 µl primary antibody solution on slide incubation over night at 4°C	min. 12h
wash in PBS	3 × 5’
clean edges (ca. 2 mm each side) position horizontally in humid compartment darken laboratory room (no sunlight)	
pipette 400 µl secondary antibody solution on slide	

incubation at room temperature under light exclusion	60’
wash in PBS	3 × 5’
position vertically in vessel, cover with DAPI solution mixing on shaking device	5’
wash in PBS	3 × 1’
mount coverslide with vectashield mounting medium	
storage under light exclusion at -20°C	

D Additional material

D.1 Illustration: Spectral filtering of Raman data

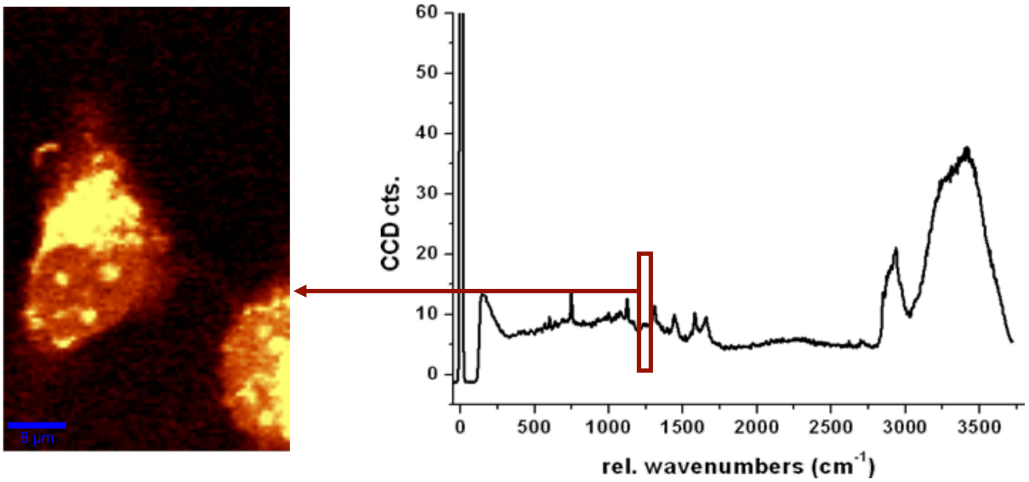

Figure D.1: *Integrated Raman spectral image generated by filtering for the region of amide III (1209-1285 cm^{-1})*

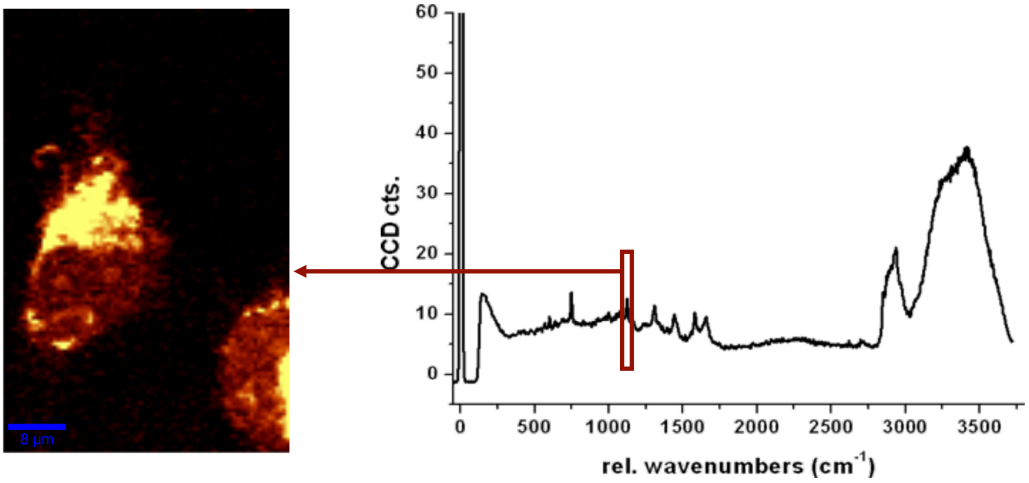

Figure D.2: *Integrated Raman spectral image generated by filtering for 1111-1136 cm^{-1} wavenumbers (region specific for C-H skeleton stretch in lipids, C-N stretch in proteins and C-O stretch in carbohydrates)*

D.2 Comparison between native and fixed cells

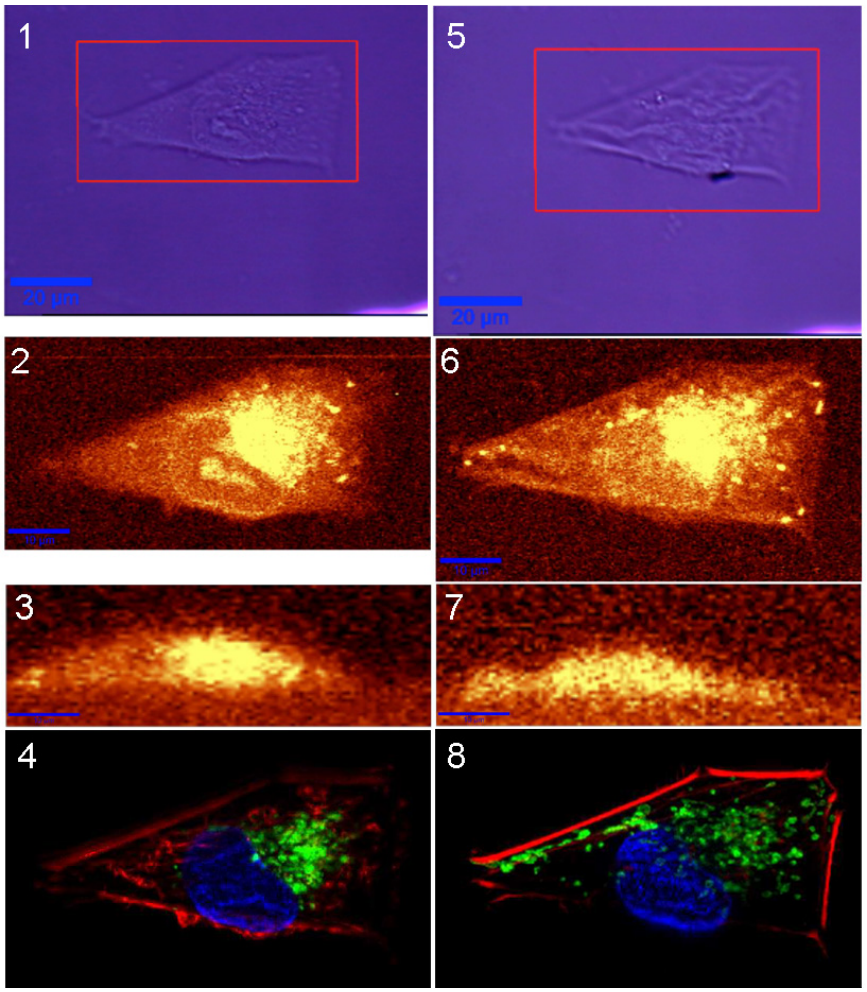

Figure D.3: *Integrated Raman spectral images of native vs. fixed cells.*

1) – 3): *Light micrograph and reconstructed Raman intensities integrated over 2800 – 3050 cm^{-1} of a living LN-18 cell*

5) – 7): *Light micrograph and reconstructed Raman intensities integrated over 2800 – 3050 cm^{-1} of the same cell after fixation in 4% phosphate buffered formalin solution*

4), 8): *Immunofluorescence images of the same, fixed, cell in different z-levels. Note the correlation to 2 and 6.*

D.3 Average spectra

Average spectrum: DMEM

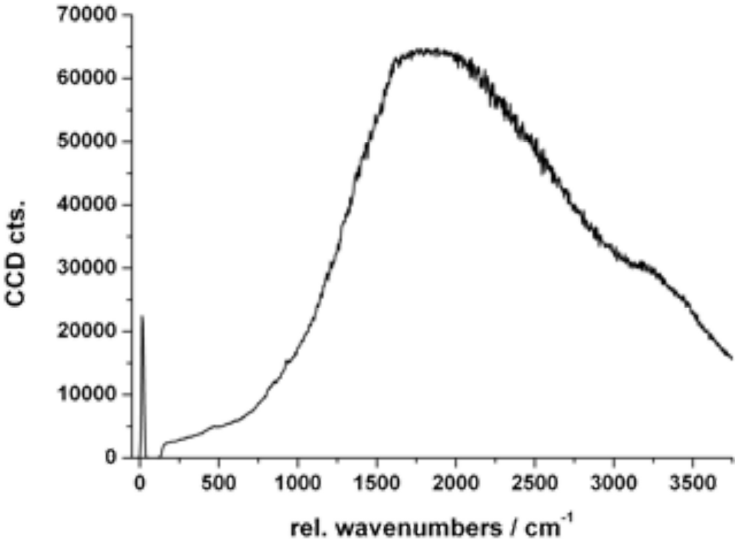

Figure D.4: *Average spectrum of dulbecco's modified eagle's medium (DMEM). Note the intensity scale.*

Average spectrum: PBS

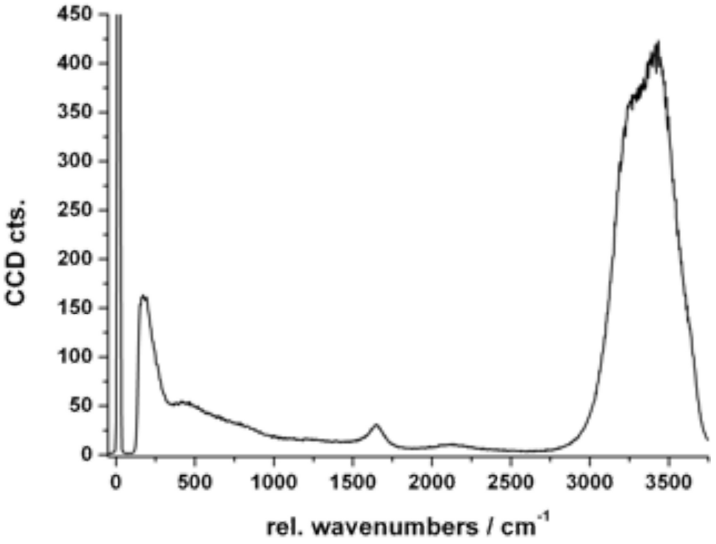

Figure D.5: *Average spectrum of phosphate buffered saline (PBS). The Raman signature originates moslty from the water component in PBS. The added salts are merely contributing to the spectrum.*

Average spectrum: glass

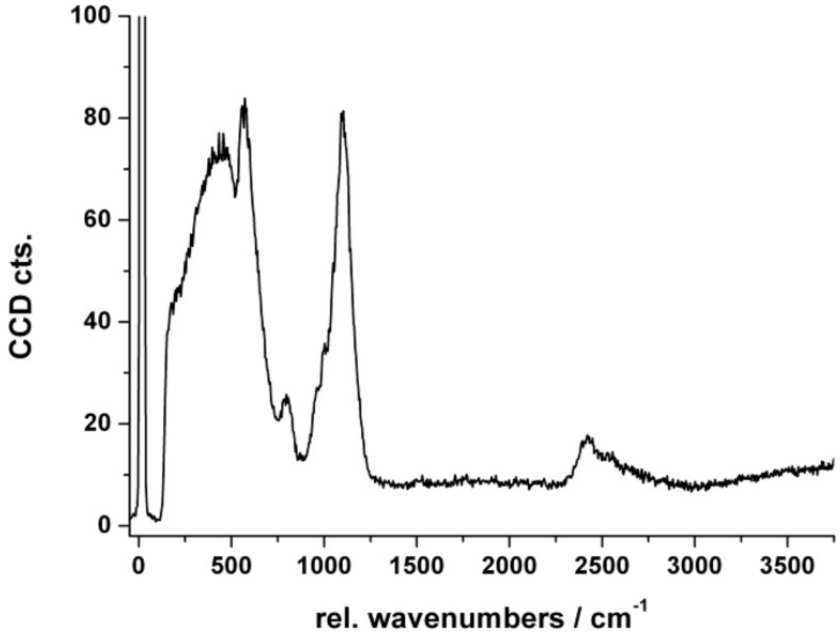

Figure D.6: *Average spectrum of a glass object slide*

D.4 List of correlation coefficents for the five channels

COMPARTMENT	MEAN	STANDARD DEVIATION	1 - SIGMA RANGE
cytoskeleton (red)	0.462	0.156	[0.306 , 0.617]
endoplasmic reticulum (green)	0.593	0.273	[0.321 , 0.866]
mitochondria (green)	0.672	0.122	[0.550 , 0.794]
Golgi apparatus (green)	0.630	0.138	[0.492 , 0.768]
nucleus (blue)	0.649	0.076	[0.573 , 0.725]
overall (RGB)	0.569	0.103	[0.466 , 0.672]

Pearsons coefficient of correlation between Raman-based aIF images and the corresponding IF counterparts: sample mean values, their standard deviation, and the 1 - sigma range given for 21 independend measurements. For the assessment of the correlation coefficients, images have been rescaled.

Eidesstattliche Erklärung

Ich erkläre an Eides statt, dass ich die der Fakultät für Medizin der Technischen Universität München zur Promotionsprüfung vorgelegte Arbeit mit dem Titel:

LABEL-FREE MICROSCOPIC BIOIMAGING BY MEANS OF CONFOCAL RAMAN SPECTROSCOPY ON LIVING GLIOBLASTOMA CELLS

im Fachgebiet Neuropathologie am Institut für Pathologie der Technischen Universität München unter der Anleitung und Betreuung durch Prof. Dr. Jürgen Schlegel ohne sonstige Hilfe erstellt und bei der Abfassung nur die gemäß § 6 Abs. 5 angegebenen Hilfsmittel benutzt habe.

Ich habe die Dissertation in dieser oder ähnlicher Form in keinem anderen Prüfungsverfahren als Prüfungsleistung vorgelegt.

Ich habe den angestrebten Doktorgrad noch nicht erworben und bin nicht in einem früheren Promotionsverfahren für den angestrebten Doktorgrad endgültig gescheitert.

Die Promotionsordnung der Technischen Universität München ist mir bekannt.

München, den 08.12.2011

Katharina Klein

Acknowledgements

Many people supported me during this work, and I want to thank them on this place.

The first person to mention is my supervisor, Prof. Dr. Jürgen Schlegel, who gave me the opportunity and time to experiment in such a challenging field which opens the limits of medical research. He constantly guided me through this work and was ready to help with any problem, still leaving me a certain freedom of work. Without him, this work could never have been carried out.

For anything concerning Raman spectroscopy and its application, I have to thank Dr. Alexander Gigler. He introduced me to the method, gave precise instructions and supported me with physical knowledge throughout the whole work.

A large part of this work has been done by Dr. Thomas Aschenbrenner, Dr. Wolfram Bunk, and Dr. Roberto Monetti. They never doubted on the feasibility of the approach and impressed our whole group with their calculations. The close collaboration has not only shown me how much teamwork can achieve, but also allowed me an insight in scientific research which I would have never thought possible.

Dr. Ferdinand Jamitzky, Prof. Dr. Gregor Morfill, and PD Dr. Robert Stark enabled this cooperation, for this I highly owe them gratitude.

Another thank goes to the group of the Division of Neuropathology of the Technical University of Munich, in particular to Guido Piontek, Ingrid Hoepner, Julian Teufel, and Andrea Schäfer, who provided the cells used for all experiments and helped me with staining protocols and fluorescence imaging. They had a great share in the solution of the biological problems.

A number of people added randomly to this work. First stands Dr. Michael Bauer, who was constantly present during the experimental part of this experiment, as well as during the formation of the work. He was always open for fruitful discussions. Likewise I am grateful to my brother Mathias, who helped me in language and LaTeX problems, and Henrik Junklewitz, with whom i could discuss all the leftover problems.
Juan Guerrero aided with pointed english corrections. Last, but not least, my mother and my friends Renato Fretta and Serena Arpe gave me moral and technical backup during the writing.